Computers and Geotechnics 134 (2021) 104060

Contents lists available at ScienceDirect

Computers and Geotechnics

journal homepage: www.elsevier.com/locate/compgeo

Research Paper

SPH-DEM simulations of saturated granular soils liquefaction incorporating particles of irregular shape

Saman Farzi Sizkow, Usama El Shamy *

Civil and Environmental Engineering Dept., Southern Methodist University, PO Box 750340, Dallas, TX 75275, United States

ARTICLE INFO

Keywords:
Discrete element method
Smoothed particle hydrodynamic
Liquefaction
Granular materials
Lateral spreading

ABSTRACT

A coupled smoothed particle hydrodynamics (SPH) and discrete element method (DEM) scheme is presented herein to investigate liquefaction of saturated granular deposits during strong seismic ground motions. Irregular-shaped solid particles in the form of polyhedral blocks are utilized to represent soil grains using DEM. In SPH, the fluid domain is discretized into distinct particles carrying local properties of the fluid. Therefore, the presented approach is a fully particle-based technique ideal for handling free-surface and moving boundary problems. The phase coupling is achieved through local averaging techniques and well-established semi-empirical relations quantifying fluid-particle interaction. Level and mildly sloped deposits were subjected to seismic ground motions introduced into the system through the base wall. The results of the performed simulations suggest that both deposits liquefied during strong base excitation due to the contraction of pore spaces leading to large increases in the excess pore fluid pressure that in turn results in significant loss of interparticle contacts and degradation of soil strength and stiffness. In addition, the sloping deposit experienced large lateral displacements, especially, at the shallow soil layers which completely liquefied during the seismic loading.

1. Introduction

The devastating effects of soil liquefaction are manifested during past major seismic events such as the 1989 Loma Prieta (California), the 1995 Kobe (Japan), the 1999 Kocaeli (Turkey), and the 2011 Christchurch (New Zealand) earthquakes (Seed et al., 1991; Erdik, 2000; Sato et al., 1995; Cubrinovski et al., 2011). Strong seismic ground motions may lead to the densification of the saturated granular deposits and reduction of the particle packing porosity. This contraction of pore space potentially results in generation of high excess pore water pressure, degradation of soil strength, and, in extreme cases, liquefaction. The onset of liquefaction is marked by the complete loss of soil strength and stiffness due to significant pore pressure build-up that counterbalances the initial confining stress at a certain depth of the deposit. Some of the recognized destructive impacts of the soil liquefaction are excessive ground settlement, tilting and sliding of structures founded on the liquefied soil due to the loss of its bearing capacity, and large horizontal ground movements, ranging up to several meters, caused by liquefaction-induced lateral spreading.

Constructing a reliable model for the coupled response of saturated granular soils as multiphase mixtures is a difficult task to undertake. The complicated nature of particle–particle and fluid-particle interactions, and constant movements of soil particles constituting the solid skeleton are some of the contributing factors to the complexity of the problem. As a result of these complications, fully continuum models used for modeling the fluid-particle systems utilize highly sophisticated plasticity constitutive models (Desai and Siriwardane, 1984; Wood, 1990; Elgamal et al., 2002; Prevost, 1985; Dafalias, 1982; Klisiński, 1988; Andrade, 2009; Seid-Karbasi and Byrne, 2007; Regueiro and Borja, 1999; Borja, 2006; Borja et al., 1999; Madabhushi and Zeng, 1998; Boulanger and Ziotopoulou, 2013; Ziotopoulou and Boulanger, 2013; Wang et al., 2014; Tasiopoulou and Gerolymos, 2016). Various meshless numerical techniques have been developed recently for large-strain problems in geotechnical engineering including landslide, liquefaction and lateral spreading. Some of these techniques are: element free Galerkin method (EFGM) (e.g., Jie et al., 2008), material point method (MPM) (e.g., Kenichi Soga et al., 2016; Yamaguchi et al., 2020), smoothed particle hydrodynamics (SPH) (e.g., Naili et al., 2005) and reproducing kernel particle method (RKPM) (e.g., Wei et al., 2020).

The discrete element method has gained widespread recognition in geotechnical engineering over the past decades as a powerful tool capable of addressing complicated issues involving simulation of

* Corresponding author.
E-mail addresses: sfarzisizkow@smu.edu (S.F. Sizkow), uelshamy@lyle.smu.edu (U. El Shamy).

https://doi.org/10.1016/j.compgeo.2021.104060
Received 11 October 2020; Received in revised form 5 February 2021; Accepted 8 February 2021
Available online 12 March 2021

discontinuous media, such as soil nonlinear behavior and non-homogeneity. It is demonstrated through numerous studies that particle surface topography, usually referred as the particle shape, can heavily affect the macro-mechanical behavior of granular media (e.g., Shin and Santamarina, 2013; Pena et al., 2007; Szarf et al., 2009; Cavarretta et al., 2010; Jiang et al., 2014; Liang and Ren, 2011). Soil grains are usually idealized as spherical particles in DEM to make the numerical simulations more manageable. However, this simplification has proven to lead to large fictitious particle rotations that in turn have significant impact on the macroscopic properties of the particle assembly such as shear strength and dilation (Zhou et al., 2013). Therefore, in order to address this issue, different techniques have been adopted to incorporate irregular-shaped particles into DEM. One approach is to incorporate rolling friction to reduce particle spinning (e.g., Bardet, 1994; Calvetti et al., 1997; El Shamy and Sizkow, 2021; Iwashita and Oda, 1998; Misra and Jiang, 1997; Oda et al., 1982). Alternatively, the grains could be modeled as polyhedron-shaped particles. For this type of particles, it is well-recognized that most of the computational effort goes into the contact detection routine and computation of the overlap length between contacting particles. Cundall (1988) presented a technique called the "common plane method" to identify the touching polyhedral blocks and to calculate the contact forces between them. Other improved versions of the common plane method were presented by other researchers (e.g., Nezami et al., 2004; Wachs et al., 2012; Nezami et al., 2006; Chang and Chen, 2008).

Several numerical schemes have been developed to simulate the fluid interaction with DEM particles. Two commonly employed techniques are: (1) using a continuum description of the fluid (e.g., El Shamy and Zeghal, 2005; El Shamy et al., 2010; Ravichandran et al., 2010) and (2) simulating the fluid at the pore scale (e.g., Zhu et al., 1999; Potapov et al., 2001; Han and Cundall, 2011; El Shamy and Abdelhamid, 2014; Abdelhamid and Shamy, 2016; Han et al., 2007; Zhong et al., 2016). The continuum-discrete description of the saturated granular deposits (FVM-DEM approach) uses a fixed coarse grid mesh which limits its scope and application to the fixed boundary problems. On the other hand, the high accuracy of the pore scale models comes at the price of being computationally expensive, to a degree that makes it impractical to perform numerical simulations with realistic particle sizes on normal desktop computers.

In recent years a new coupled SPH-DEM scheme has been developed that, instead of modeling the fluid flow at the pore scale, uses averaged Navier–Stokes equations to describe the fluid phase behavior and well-established semi-empirical formulas for fluid-particle interactions. Due to the meshless nature of the SPH-DEM technique, it can relatively easily analyze fluid–structure interaction problems where, for example, FVM-DEM has some obvious limitations. Sun et al. (2013) presented a Lagrangian-Lagrangian SPH-DEM coupled model for the multiphase flows with free surfaces. They performed dam break and rotational cylindrical tank simulations to showcase the proposed method abilities. Robinson et al. (2014) presented a meshless simulation technique based on coupled SPH-DEM algorithm and validated the model by conducting simulations of single particle and constant porosity block sedimentation in a fluid column. Many more examples of coupled SPH-DEM application to various chemistry, physics and engineering problems can be found in the recent literature (e.g., (Markauskas et al., 2018; Markauskas and Kruggel-Emden, 2019; Fernandez et al., 2011; Sinnott et al., 2017; Cleary, 2015; Karunasena et al., 2014; Wu et al., 2016)).

Different researchers have investigated soil liquefaction phenomenon using DEM. Most of these studies are concerned with the undrained behavior of saturated granular soil subjected to monotonic or cyclic shearing (Johnson et al., 2017; El Shamy and Denissen, 2010; Huang et al., 2019; Foroutan and Mirghasemi, 2020; Salimi and Lashkari, 2020; Gu et al., 2020; Wang et al., 2019; Huang et al., 2020; Gong et al., 2012; Martin et al., 2019; Kuhn et al., 2014; Ng and Dobry, 1994; Sitharam et al., 2009; Wang and Wei, 2016; Wei et al., 2018; Shafipour and Soroush, 2008). Two main approaches used for this purpose are the fluid-particle coupling methods and the constant volume technique. The constant volume method can only be employed for a specimen under undrained condition and the presence of the fluid is indirectly accounted for by controlling the displacements at the boundaries to keep the specimen volume constant. Apart from liquefaction under undrained conditions, to the best of authors' knowledge, there have only been few studies regarding the soil liquefaction using DEM coupled with an actual pore-fluid model (e.g., El Shamy and Zeghal, 2005; El Shamy et al., 2010; El Shamy and Abdelhamid, 2014).

This paper presents the results of a soil liquefaction model using a coupled SPH-DEM algorithm. In this method, the soil is modeled at the microscale level as an assembly of polyhedral rigid blocks using DEM and SPH is utilized to solve the fluid phase equations. It is assumed that the averaged Navier–Stokes equations govern the fluid behavior and the interaction forces between fluid and solid particles are quantified through well-known semi empirical relationships. The proposed approach was used to investigate the responses of level and sloping saturated granular deposits to low and high amplitude base excitations. The obtained results suggest that liquefaction is a result of reduction in void spaces during strong ground motions leading to high pore pressure buildup and consequent loss of interparticle contacts and degradation of soil strength and stiffness. Furthermore, the liquefied top layers in the sloping deposit experienced large lateral displacement due to the inertia force component in the downslope direction.

2. Coupled SPH-DEM model

A fully Lagrangian particle-based method is presented herein to analyze the dynamic response of saturated granular deposits subjected to horizontal seismic base excitations. In SPH scheme, the fluid domain is discretized into a set of individual particles carrying local properties of the fluid such as density and pressure (Gingold and Monaghan, 1977; Lucy, 1977; Monaghan, 1992). A SPH kernel function is utilized to interpolate the averaged forms of continuity and momentum equations over all neighboring particles within the smoothing length of a given point. The fluid pressure is obtained from the weakly compressible equation of state. Therefore, a large value is assigned to the speed of sound to ensure negligible fluctuations in the fluid density. The phase coupling is achieved through semi-empirical relationships between the fluid-particle interaction forces and parameters such as the local porosity and relative velocity between the two phases. These interaction forces are directly applied to the solid particles as external forces and are accounted for in the fluid phase formulation by adding an associated term to the momentum equation. An explicit time integration scheme is used to solve the equation of motion for both solid and fluid particles. Model components are described in detail in the following sections.

2.1. Fluid phase

The two-fluid model presented by Anderson and Jackson (1967) is used here to describe the governing equations for the multiphase mixture (Robinson et al., 2014):

$$\frac{\partial(n\rho_f)}{\partial t} + \nabla.(n\rho_f \mathbf{u}) = 0 \tag{1}$$

$$\frac{\partial(n\rho_f \mathbf{u})}{\partial t} + \nabla.(n\rho_f \mathbf{u}\mathbf{u}) = -\nabla P + \nabla.\boldsymbol{\tau} + n\rho_f \mathbf{g} - \mathbf{f}^{\mathbf{int}} \tag{2}$$

in which ρ_f is the fluid density, n is the porosity, P is the fluid pressure, $\boldsymbol{\tau}$ is the viscous stress tensor, $\mathbf{f}^{\mathbf{int}}$ is the fluid particle interaction force, $\mathbf{g}$ is the gravitational acceleration vector and $\mathbf{u}$ is the fluid velocity.

The SPH formulation is based on the mathematical principle of interpolant integration. This principle states that a field quantity A at the location $\mathbf{r}$ can be approximated through convolution with the smoothing function W:

$$A(\mathbf{r}) = \int_{\Omega} A(\mathbf{r}')W(\mathbf{r}-\mathbf{r}', h)d\mathbf{r}' \tag{3}$$

where h is the smoothing length and Ω is the surrounding volume. In SPH, the continuum is lumped into discrete particles moving with the flow velocity and each holding information regarding the physical properties of the fluid. Therefore, in a further approximation, the interpolant integral of Eq. **(3) is transformed into the summation of weighted contribution of all particles inside the supporting domain of particle i:

$$A_i = \sum_j A_j \frac{m_j}{\rho_j} W(|\mathbf{r_{ij}}|, h) \tag{4}$$

where $|\mathbf{r_{ij}}|$ is the distance between two particles, m_j is the mass of particle j and ρ_j is the density of particle j. To avoid confusion, hereafter, the subscripts i and j are used for the SPH particles and a and b indicate the DEM particles. In this study the Wendland kernel function is chosen as the smoothing function (Dehnen and Aly, 2012):

$$\begin{cases} W(|\mathbf{r}|, h) = \alpha_D (1-\frac{q}{2})^4 (1+2q) & 0 \leqslant q \leqslant 2 \\ 0 & 2 < q \end{cases} \tag{5}$$

in which $q = \frac{|\mathbf{r}|}{h}$ and $\alpha_D = \frac{21}{16\pi h^3}$. Applying SPH particle summation, Eqs. **(1) and (2) can be rewritten as:

$$\frac{d(n_i\rho_i)}{dt} = \sum_j m_j \mathbf{u_{ij}}.\nabla_i W(|\mathbf{r_{ij}}|, h) \tag{6}$$

$$\frac{d\mathbf{u_i}}{dt} = -\sum_j m_j \left[\frac{P_i}{(n_i\rho_i)^2} + \frac{P_j}{(n_j\rho_j)^2} + R_{ij}\left(\frac{W(|\mathbf{r_{ij}}|, h)}{W(\Delta p, h)}\right)^4\right]\nabla_i W(|\mathbf{r_{ij}}|, h) + \mathbf{\Pi}_{ij} + \frac{\mathbf{f^{int}}}{m_i} + \mathbf{g} \tag{7}$$

with $\mathbf{u_{ij}}$ being the relative velocity vector, P_i fluid pressure evaluated at the location of particle i, R_{ij} the tensile instability term to prevent particles from forming small clumps and $\mathbf{\Pi}_{ij}$ the non-artificial viscosity term. R_{ij} and $\mathbf{\Pi}_{ij}$ are defined as (Morris et al., 1997; Monaghan, 2000):

$$\mathbf{\Pi}_{ij} = \sum_j \frac{m_j(\mu_i + \mu_j)\mathbf{r_{ij}}.\nabla_i W(|\mathbf{r_{ij}}|, h)}{\rho_i\rho_j(|\mathbf{r_{ij}}|^2 + 0.01h^2)}\mathbf{u_{ij}} \tag{8}$$

$$R_{ij} = \begin{cases} 0.01\left[\frac{P_i}{(n_i\rho_i)^2} + \frac{P_j}{(n_j\rho_j)^2}\right] & P_i > 0 \text{ and } P_j > 0 \\ 0.2\left[\left|\frac{P_i}{(n_i\rho_i)^2}\right| + \left|\frac{P_j}{(n_j\rho_j)^2}\right|\right] & \text{otherwise} \end{cases} \tag{9}$$

The porosity at the position of a fluid particles can be estimated by particle summation over all DEM particles present within its kernel radius:

$$n_i = 1 - \sum_a W(|\mathbf{r_{ai}}|, h)V_a \tag{10}$$

in which $|\mathbf{r_{ai}}|$ is the distance between fluid particle i and DEM particle a and V_a is the volume of the DEM particle. The weakly compressible equation of state is used to calculate the fluid pressure. This equation provides a relationship between the fluid pressure and its density (Monaghan, 1994):

$$P_i = B\left(\left(\frac{\rho_i}{\rho_0}\right)^{\gamma} - 1\right) \tag{11}$$

where ρ_0 is the reference density, B is the pressure constant and $\gamma = 7$. In order to minimize the density variations and to keep the fluid behavior as close as possible to incompressible, the proper value for B must be determined. B is defined in terms of the local sound speed c_s as:

$$B = \frac{\rho_0 c_s^2}{\gamma} \tag{12}$$

The variations in the fluid density can be obtained from (Monaghan, 1994):

$$\frac{|\Delta\rho_i|}{\rho_0} = \frac{|\mathbf{u_i}|^2}{c_s^2} = M^2 \tag{13}$$

where $\mathbf{u_i}$ is the fluid velocity and M is the Mach number. Therefore, the numerical speed of sound is usually considered to be 10 times higher than the maximum fluid velocity to limit the fluctuations of the fluid density to less than 1% of its initial value.

Up to now, several boundary treatment techniques have been proposed to enforce no-slip, impenetrable conditions including dummy boundary particles with repulsive forces, mirror particles, fluid particles that move with the boundary and the application of distance functions (Monaghan, 1994; Randles and Libersky, 1996; Chen et al., 1999; Crespo et al., 2007; Gómez-Gesteira et al., 2005; Sun et al., 2013). In this paper, the solid boundaries for SPH particles are treated in the same manner as described by Adami et al. (2012). In this approach, the solid boundary is represented by two layers of dummy particles. These particles compensate for the domain truncation near the boundary and provide kernel support for the adjacent fluid particles. To ensure no-slip boundary condition the velocities of the dummy particles are extrapolated from the surrounding fluid particles:

$$\mathbf{u_w} = 2\mathbf{u_0} - \tilde{\mathbf{u}}_\mathbf{w} \tag{14}$$

$$\tilde{\mathbf{u}}_\mathbf{w} = \frac{\sum_j \mathbf{u_j} W(|\mathbf{r_{wj}}|, h)}{\sum_j W(|\mathbf{r_{wj}}|, h)} \tag{15}$$

in which $\mathbf{u_0}$ is the prescribed wall velocity. In addition, in order for the dummy particles to produce correct pressure gradient near the boundary, the pressure and density of wall particles should also be calculated from the neighboring fluid particles:

$$P_w = \frac{\sum_j P_j W(|\mathbf{r_{wj}}|, h) + (\mathbf{g} - \mathbf{a_w}).\sum_j \rho_j \mathbf{r_{wj}} W(|\mathbf{r_{wj}}|, h)}{\sum_j W(|\mathbf{r_{wj}}|, h)} \tag{16}$$

$$\rho_w = \rho_0\left(\frac{P_w}{B} + 1\right)^{\frac{1}{\gamma}} \tag{17}$$

Periodic boundaries represent a condition where the domain is extended infinitely on the sides. The implementation of this type of boundary condition is rather straight forward in SPH. In this case, the two sides of the model are considered adjacent to each other and, therefore, the truncated support domain of a particle close to one side is completed by contributing particles on the opposite side. In addition, if a particle crosses a periodic boundary it will re-enter the domain from the other side with the same velocity.

2.2. Solid phase

The discrete element method was used to model the soil deposits. In DEM the most common approach is to idealize the soil grains as rigid spherical bodies to reduce the computational cost and eliminate the complexities arising from irregular particle shapes. However, this simplification may produce highly inaccurate rotational inertia which is proven to have major impact on the energy dissipation during rotational movements of particles and micromechanical behavior of the granular materials (Bardet and Huang, 1992; Bardet, 1994; Iwashita and Oda, 1998; Oda et al., 1982; Calvetti et al., 1997; Misra and Jiang, 1997). Therefore, naturally, an assemblage of irregular-shaped blocks can be

the most realistic representation of a soil deposit. In this study, rigid blocks, as described by Itasca (2018), are used to create the non-spherical particles.

A rigid block is a closed, convex-shaped body composed of multiple triangular facets. Each rigid block is treated as a single piece, meaning there can only be one contact point between two rigid blocks or between a rigid block and a wall. Non-sphericity of these particles eliminates the need for application of rolling friction, and therefore, the linear elastic contact model suffices to describe their interaction. The contact detection between rigid blocks are done using the Gilbert-Johnson-Keerthi (GJK) algorithm (Ong and Gilbert, 1997) which is an iterative method that uses Minkowski difference to find the overlapping particles. That is, two convex bodies are in contact if the origin is located inside the constructed Minkowski difference of them. For contacts between wall facets and rigid blocks, a point at the center of the facet is added to the collection of points used in the GJK algorithm. After detecting the overlaps, the contact point located at the centroid of the overlap volume must be determined to compute the associated contact forces. This is done using the method presented by Shamos and Hoey (1976).

2.3. Fluid–solid interaction

The total force exerted by the fluid on the solid particle a can be written as the sum of the drag force ($\mathbf{F_a^D}$) and pressure gradient force ($\mathbf{F_a^P}$) (Markauskas et al., 2017):

$$\mathbf{F}_a^{\mathbf{int}} = \mathbf{F_a^D} + \mathbf{F_a^P} \tag{18}$$

The drag force can be estimated through a verity semi-empirical relationships. The well-known equation recommended by Ergun (1952) was used in this study. This equation evaluates the drag force based on the local porosity and the relative velocity between fluid and solid particles and was developed using hundreds of experimental results on spherical and non-spherical particles:

$$\mathbf{F_a^D} = \frac{\beta V_a}{1-n_a}(\bar{\mathbf{u}}_\mathbf{a} - \mathbf{u_a}) \tag{19}$$

where β is the interphase momentum exchange coefficient, $\bar{\mathbf{u}}_\mathbf{a}$ is the average flow velocity around the solid particle a, V_a is the volume of the solid particle, $\mathbf{u_a}$ is the velocity of the solid particle and n_a is the mean porosity. The average flow velocity can be calculated by interpolating the nearby fluid particle velocities as:

$$\bar{\mathbf{u}}_\mathbf{a} = \frac{\sum_j \mathbf{u}_j \frac{m_j}{\rho_j} W(|\mathbf{r_{aj}}|, h)}{\sum_j \frac{m_j}{\rho_j} W(|\mathbf{r_{aj}}|, h)} \tag{20}$$

The mean porosity at the location of a solid particle can also be estimated from the porosities of the surrounding SPH particles:

$$n_a = \frac{\sum_j n_j \frac{m_j}{\rho_j} W(|\mathbf{r_{aj}}|, h)}{\sum_j \frac{m_j}{\rho_j} W(|\mathbf{r_{aj}}|, h)} \tag{21}$$

β follows two different regimes devided by the local porosity ranges (Ergun, 1952):

$$\beta = \begin{cases} 150\frac{(1-n_a)^2}{n_a}\frac{\mu}{d_a^2} + 1.75(1-n_a)\frac{\rho}{d_a}|\bar{\mathbf{u}}_\mathbf{a} - \mathbf{u_a}| & n_a \leqslant 0.8 \\ 0.75 C_d \frac{n_a(1-n_a)}{d_a}\rho|\bar{\mathbf{u}}_\mathbf{a} - \mathbf{u_a}| n_a^{-2.65} & n_a > 0.8 \end{cases} \tag{22}$$

in which μ is the dynamic viscosity of the fluid, d_a is the equivalent diameter of the solid particle and C_d is the drag coefficient given by:

$$C_d = \begin{cases} \frac{24}{Re_a}(1 + 0.15 Re_a^{0.687}) & Re_a \leqslant 1000 \\ 0.44 & Re_a > 1000 \end{cases} \tag{23}$$

Re_a is the particle Reynolds number that can be calculated from (Trussell and Chang, 1999):

$$Re_a = \frac{|\bar{\mathbf{u}}_\mathbf{a} - \mathbf{u_a}| n_a \rho d_a}{\mu} \tag{24}$$

If the interaction between fluid and solid particles is the only source for the generation of pressure gradient, the total interaction force can be simplified as (Markauskas et al., 2017):

$$\mathbf{F}^{\mathbf{int}_a} = \mathbf{F_a^D} + \mathbf{F_a^P} = \frac{\mathbf{F_a^D}}{n_a} - V_a \rho_f \mathbf{g} \tag{25}$$

Due to the momentum exchange with solid particles, a coupling force will also be applied to the fluid particle i which can be estimated by the weighted average of contributions from all surrounding DEM particles inside its influence domain:

$$\mathbf{f}_i^{\mathbf{int}} = -\frac{m_i}{\rho_i}\sum_a \frac{W(|\mathbf{r_{ai}}|, h)}{\sum_j \frac{m_j}{\rho_j} W(|\mathbf{r_{aj}}|, h)} \mathbf{F}_a^{\mathbf{int}} \tag{26}$$

2.4. Computational scheme

The PFC3D software was used to handle the DEM calculation cycles (Itasca, 2018). The SPH part of the coupled algorithm was carried out by a Cython code written by the authors and linked to the PFC3D environment. Use was made of the Open Multi-Processing (OpenMP) technology to parallelize the SPH code and reduce the computational time. Note that the DEM software already utilizes parallel computing. In addition, to accelerate the neighbor searching process, the fluid domain was divided into cubic cells with sides at least two times larger than the kernel radius (h). All DEM and SPH particles were then mapped into these cells. This way, only a maximum of 27 cells were needed to be probed to find all particles within the support domain of any given SPH particle. Special attention must be paid to the cell size. Using larger cells leads to having more particles inside each cell and slower neighbor searching routines. However, on the other hand, it reduces the number of particle mapping updates required during the simulation. Therefore, an optimum cell size creates a balance between the time spent in a single neighbor searching process and the frequency of particle mapping.

The fluid and solid phase equations were solved using explicit time integration schemes. A constant value was selected for the DEM timestep. This value must be smaller than the critical DEM timestep to guarantee stable simulations. The SPH timestep must also satisfy several timestep criteria including CFL condition (Morris et al., 1997) and is usually larger than the DEM timestep. Therefore, the SPH timestep was assumed to be N times the DEM timestep, where N is an integer. This means that N DEM computation cycles should be performed per one SPH cycle. The first step in a single SPH-DEM computational loop is to calculate the fluid particle properties such as porosity and pressure. The interaction forces are next obtained based on the latest positions and velocities of DEM particles, and the interpolated porosities at their locations. Then the SPH particle densities, velocities and positions are updated according to the variation rates of density and velocity computed from their pressure, superficial density and the coupling forces. Finally, the interaction forces are applied to the solid particles and N DEM cycles are performed to get the updated particle positions and velocities. The new positions and velocities are then sent as inputs to the SPH algorithm and the next loop begins.

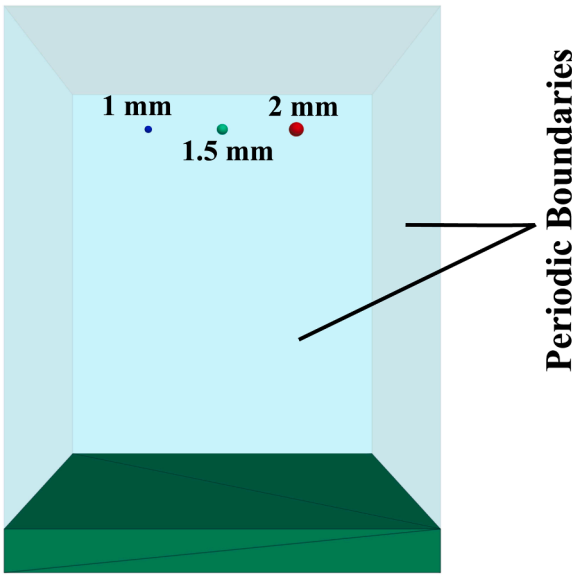

Fig. 1. Initial setup for particle sedimentation test.

3. Validation cases

In view of the complexity of the goal of this study to model soil liquefaction of a saturated soil deposit, a building block approach was adopted herein to validate the proposed coupled SPH-DEM model. The main coupling parameters between the fluid and particles in this model stem from porosity calculation, averaged solid particle velocities and the resulting drag force. Therefore, a simulation was performed to examine the ability of the model to correctly predict the drag force on a few settling particles in a fluid column. Since this system has a diluted concentration of particles, it presents an extreme in computing porosity and associated drag forces. It also include the challenge of large solid particle velocities. Additionally, another extreme situation in which flow in a dense stagnant arrangement of a porous medium was considered to examine the ability of the fluid code to accurately predict fluid velocities in such a dense packing.

3.1. Particle sedimentation

Particle sedimentation test was performed to examine the accuracy of the coupled SPH-DEM algorithm. A fluid column with dimensions of $4.8 \times 4.8 \times 6$ cm was created using SPH particles with initial spacing of 4 mm, density of 10^3 kg/m^3 and dynamic viscosity of 5.0 Pa.s. Three solid particles with density of 2×10^3 kg/m^3, and radii of 0.5 mm, 0.75 mm and 1 mm were placed within the fluid domain and allowed to settle under the gravitational acceleration of 9.81 m/s^2 (Fig. 1). Assuming $n_a \approx 1$ and $Re \ll 1$, the drag force can be calculated from Eqs. **(19), (22), (23) and (24) as:

$$F_z^D = 3\pi\mu d_a v_z \tag{27}$$

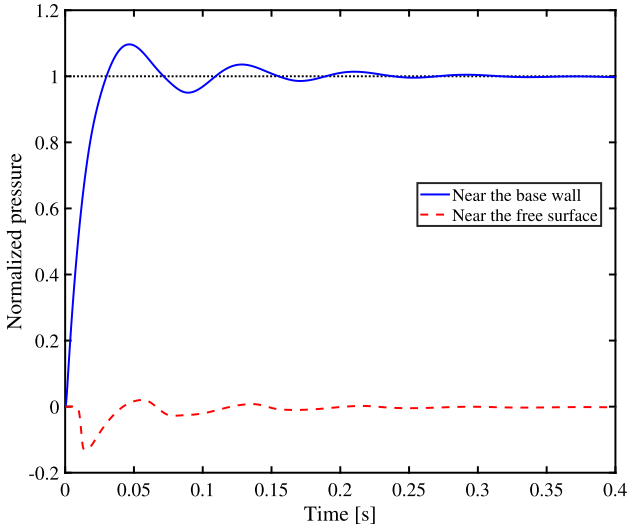

Fig. 3. Normalized pressure time histories at two different locations along the fluid column.

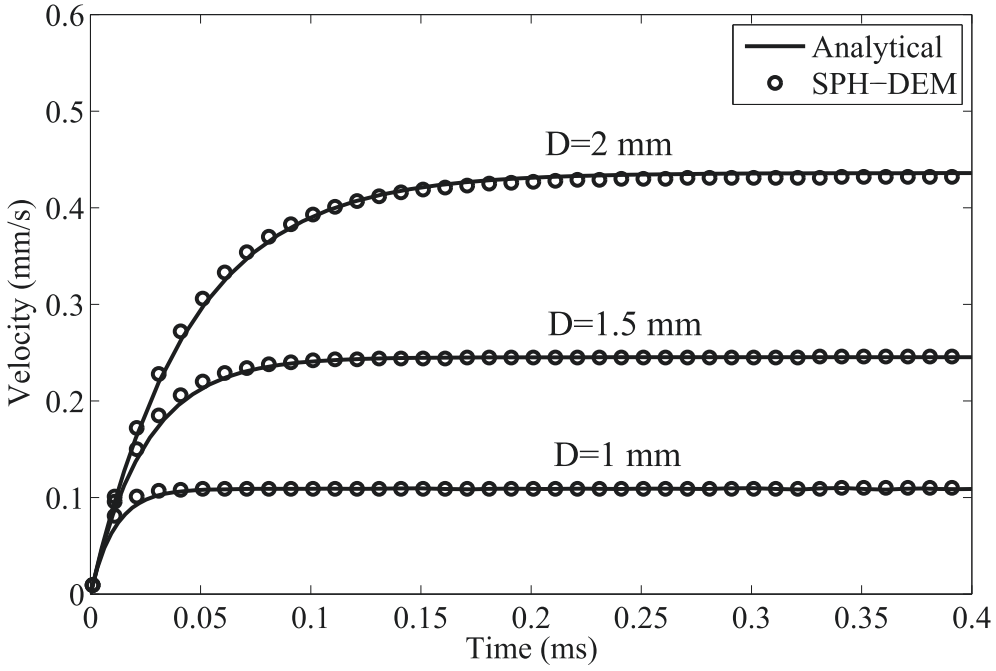

Fig. 2. Comparison between the analytical and numerical results for the vertical velocities of the particles.

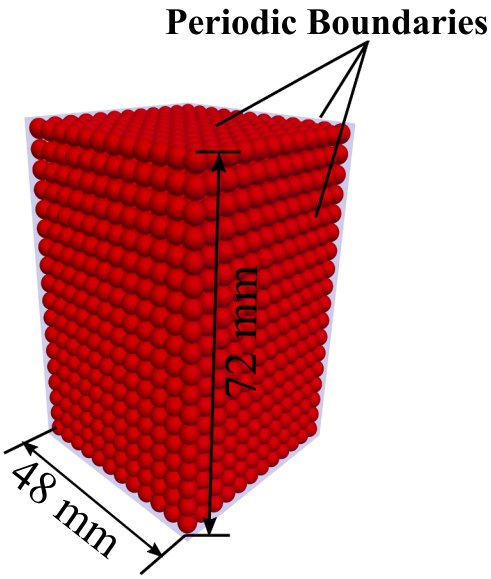

Fig. 4. Porous block model (only DEM particles are illustrated).

Using Eq. **(27) and solving the differential equation obtained from Newton's second law, the velocity of a falling particle inside a fluid can be computed by:

$$v_z(t) = \frac{2(\rho_p - \rho_f)gr^2}{9\mu}[1 - exp(-\frac{-9\mu t}{2(\rho_p - \rho_f)r^2})] \quad (28)$$

where ρ_p and ρ_f are solid and fluid particle densities, μ is the dynamic viscosity, r is the solid particle radius and g is the vertical gravitational acceleration. Fig. 2 shows a close agreement between the results of numerical and analytical solutions. Fig. 3 shows the transient average pressures normalized by the total weight of particles divided by the cross-sectional area of the water column at two different points: one near the base wall and one near the top of the container (hydrostatic pressure is neglected here). It can be observed that the normalized pressure at the point near the base underwent a relatively small fluctuations before reaching the value of one. The pressure near the free surface also experienced some fluctuations and returned to zero.

3.2. Flow through a porous block

In this test a submerged cubic packing of identical solid particles was created within a three-dimensional periodic box. That is, the boundary conditions for both DEM and SPH particles were considered to be periodic in all three directions. The diameter of the solid particles was 2 mm and the periodic box had the dimensions of 4.8 × 4.8 × 7.2 cm (Fig. 4). The analytically calculated porosity of the cubic packing is approximately 47.6%. The domain was filled with SPH particles with densities of 10^3 kg/m^3 and an initial distance of 4 mm. The fluid particles were subjected to constant body forces of 1 m/s^2 in the vertical direction. A range of particle Reynolds numbers was achieved by varying the fluid dynamic viscosity between 0.0001 Pa.s and 0.04 Pa.s. The friction factor (f_p) inside a packed assembly of particles can be related to the modified particle Reynolds number Gr_p by (Ergun, 1952):

$$f_p = \frac{150}{Gr_p} + 1.75 \quad (29)$$

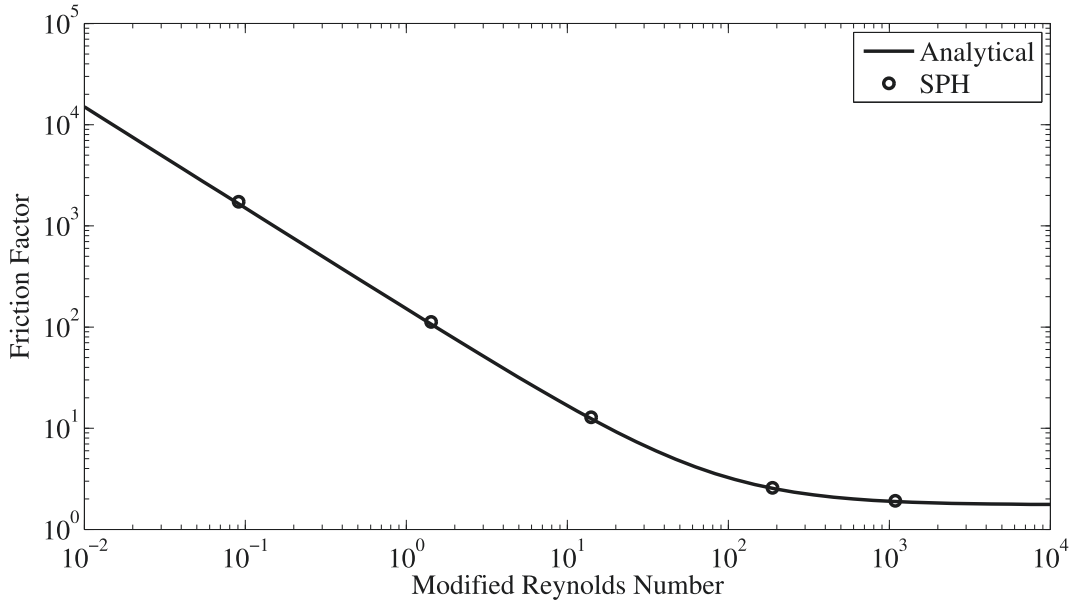

Fig. 5. Friction factor as a function of modified Reynolds number obtained from the analytical and numerical solutions.

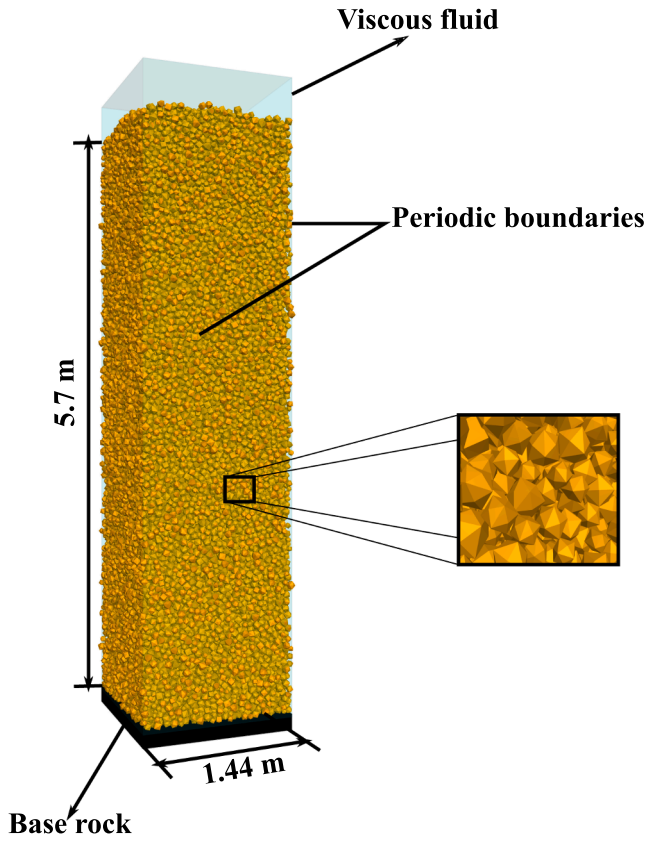

Fig. 6. 3D view of the saturated granular deposit.

The friction factor and modified Reynolds number are defined as:

$$f_p = \frac{\Delta P}{H}\frac{d_p}{\rho v_s^2}\left(\frac{n^3}{1-n}\right) \tag{30}$$

$$Gr_p = \frac{\rho v_s d_p}{(1-n)\mu} \tag{31}$$

where ΔP is pressure drop, n is the porosity, d_p is solid particle diameter, H is height of the column, ρ is fluid density, v_s is the superficial fluid velocity and μ is dynamic viscosity. A comparison between the numerical and analytical solutions is provided in Fig. 5. This figure shows that the results are compatible for a wide range of Reynold numbers.

4. Liquefaction of saturated granular soil

The validated coupled SPH-DEM approach was used to analyze the response of level and mildly sloped saturated granular deposits to seismic base excitations. Periodic boundaries were employed at four sides of the model for both DEM and SPH particles to simulate an infinite medium with a limited number of particles. In addition, use was made of the high g-level concept commonly used in centrifuge testing to further decrease the dimensions of the domain that needed to be filled with particles and benefit from a shorter simulation time (Iai et al., 2005). This approach was found to be very effective in DEM simulations to model boundary value problems and has been adopted in several applications (e.g., El Shamy and Zeghal, 2005; El Shamy and Aydin, 2008). The lower boundary represents the bedrock and was modeled by a rigid wall in DEM and by a no-slip, impermeable boundary in SPH. One of the advantages of the SPH method is its ability to simulate free surface boundaries without the need of special treatments. Therefore, the free surface condition is automatically applied to the top boundary by filling the domain with fluid particles. The seismic excitations were applied to the fluid and solid phases through the base boundaries. A detailed description of the model and its components is provided in the following section.

Table 1
Simulations details in model units.

Soil deposit	
Particle size	1.5 mm to 2.5 mm
Normal stiffness	5.0×10^5 N/m
Shear stiffness	5.0×10^5 N/m
Normal critical damping ratio	0.1
Shear critical damping ratio	0.0
Friction coefficient	0.5
Rolling friction coefficient	0.2
Density	2650 kg/m^3
Number of particles	56,000
Viscous Fluid	
Initial spacing	4 mm
Kernel radius	5 mm
Dynamic viscosity	0.6 Pa.s
Density	1000 kg/m^3
Computation parameters	
g-level	30
Time step for DEM	6×10^{-7} s
Time step for SPH	6×10^{-6} s

4.1. Model description

The simulations were conducted on 190 mm high (in model units) level and sloping deposits. The lateral dimensions of the periodic deposits were chosen to be 48 × 48 mm. The deposits were created using polyhedral blocks with equivalent diameters ranging from 1.5 mm to 2.5 mm which is close to coarse sand grain size. The average sphericity of the particles used in this study was determined to be approximately 0.98. First, the approximate number of particles needed to fill the domain was calculated. Then these particles were generated in a relatively large space and allowed to settle under high gravitational field of 30 g. The porosity of the final assembly can be controlled by applying different values to the local damping and/or adjusting the friction coefficient during the particle settlement process. The average porosity and saturated unit weight of the deposits were determined to be, respectively, around 43% and 19.4 kg/m^3.

To saturate the deposits, a fluid domain with a height of 200 mm and lateral dimensions of 48 × 48 mm was introduced within the periodic domain using SPH particles. The initial spacing of the fluid particles and the kernel radius were chosen to be 4 mm and 5 mm, respectively. A 3D view of the saturated level deposit is shown in Fig. 6. The ratio between the smoothing length (h) and the average particle diameter (d) can have significant effects on the accuracy of the numerical simulations. Robinson et al. (2014) conducted single particle and porosity block sedimentation tests using a coupled SPH-DEM algorithm and concluded that a kernel radius of $h \geqslant 2d$ leads to a smooth porosity field, however, the model can suffer from too strong smoothing and the ensuing errors if a considerably higher value is used. The parameters used in the following simulations gives a ratio of $h/d = 2.5$, which is within the optimum range. Note that the same kernel radius was used in the two validation simulations discussed in Section 3, in which two extreme porosity cases

Table 2
Amplification factors obtained from DEM solution and analytical expression.

Input Frequency (Hz)	Amplification Factor (DEM)	Amplification Factor (Analytical)
3	2.03	2.08
4	5.68	6.43
5	4.1	4.24
6	2.37	1.79

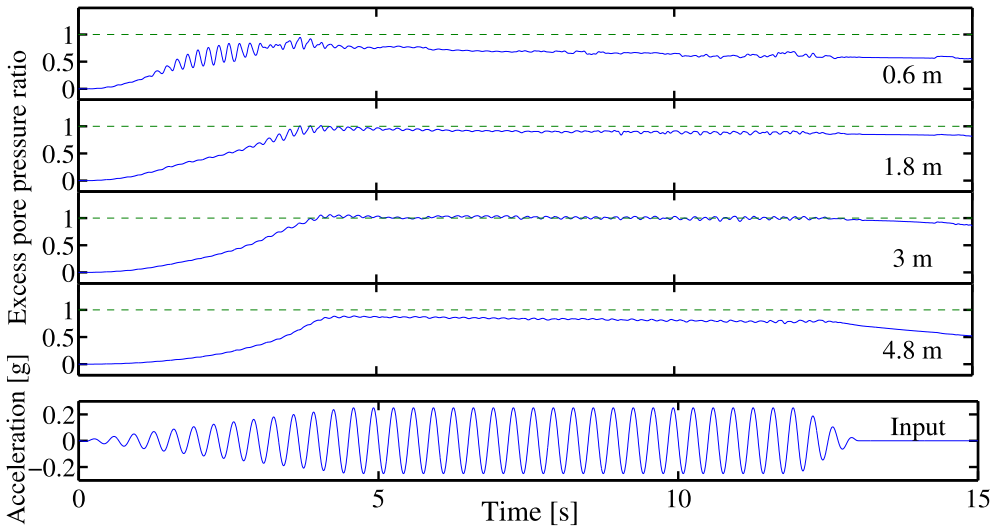

Fig. 7. Time histories of excess pore water pressure at the selected depth locations (level deposit).

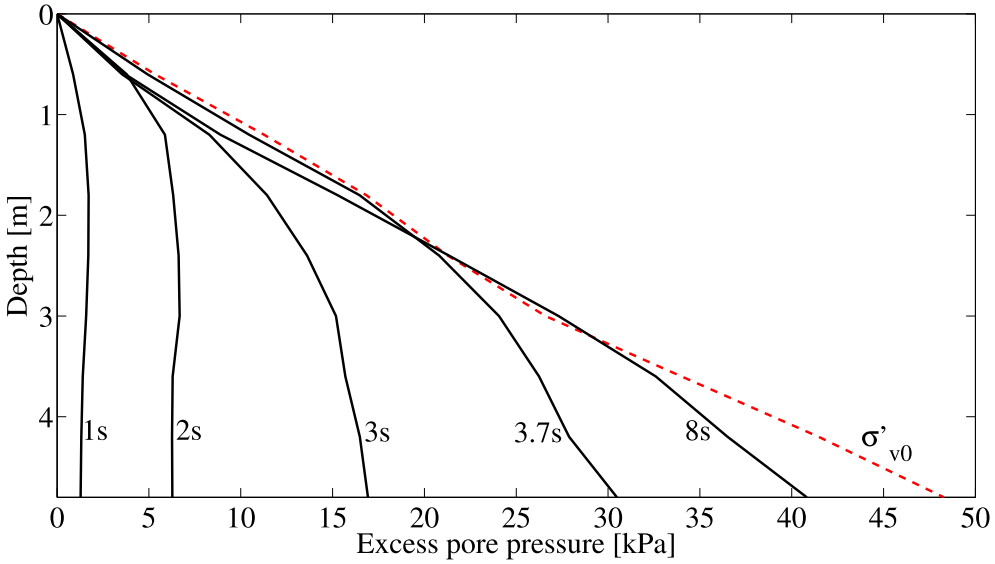

Fig. 8. Excess pore pressure profiles at the selected time instants (level deposit).

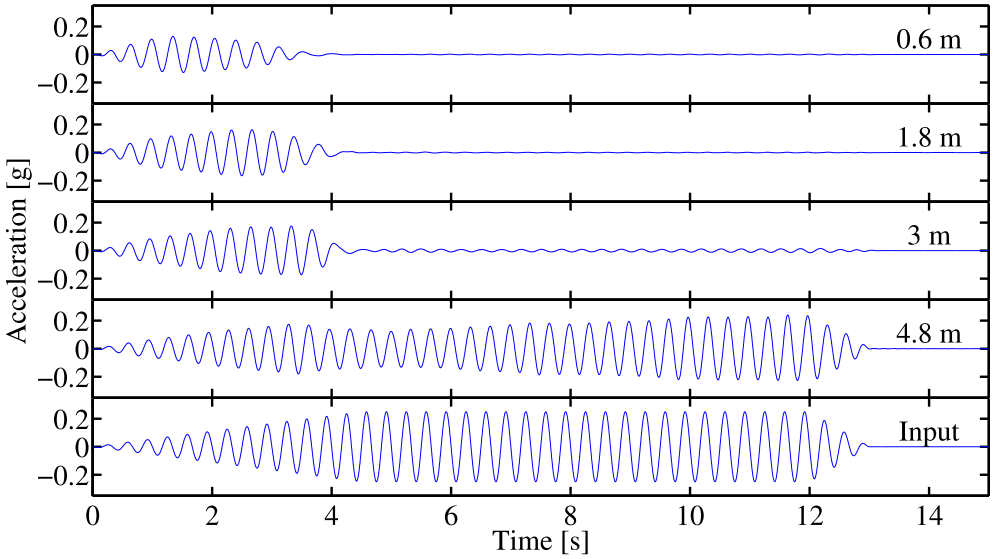

Fig. 9. Time histories of average horizontal acceleration at the selected depths (level deposit).

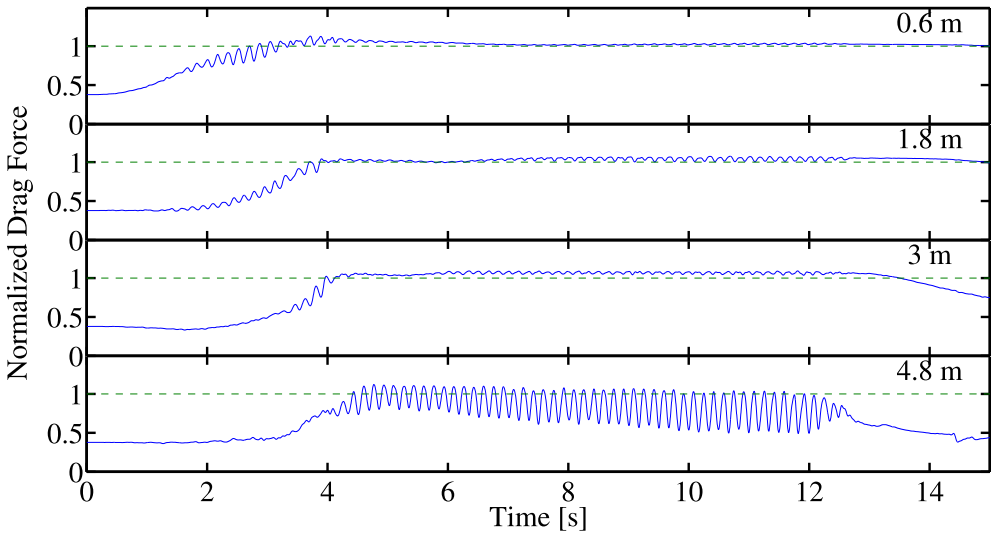

Fig. 10. Time histories of vertical fluid drag force normalized by the average particle weight at the selected depths (level deposit).

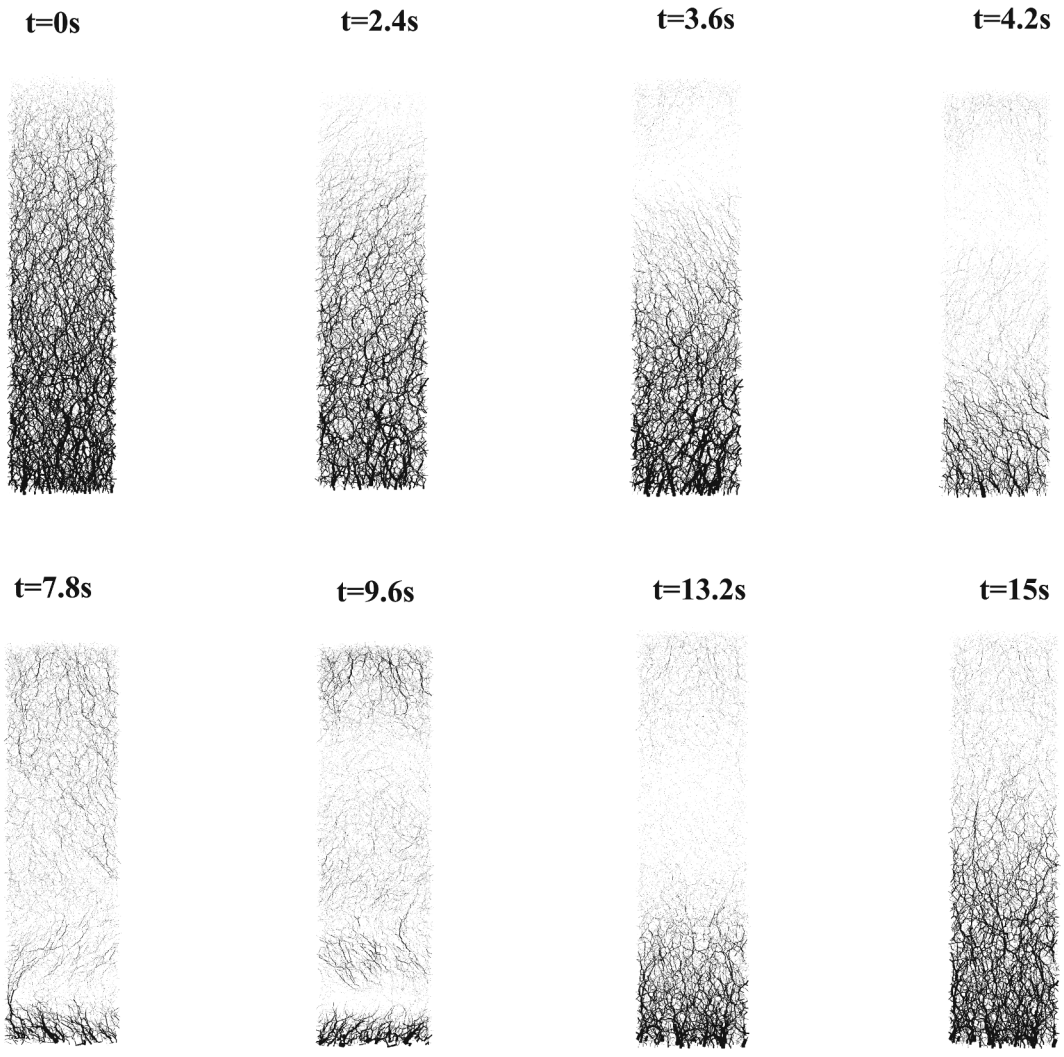

Fig. 11. Snapshots of interparticle contact chain at different time instants (level deposit).

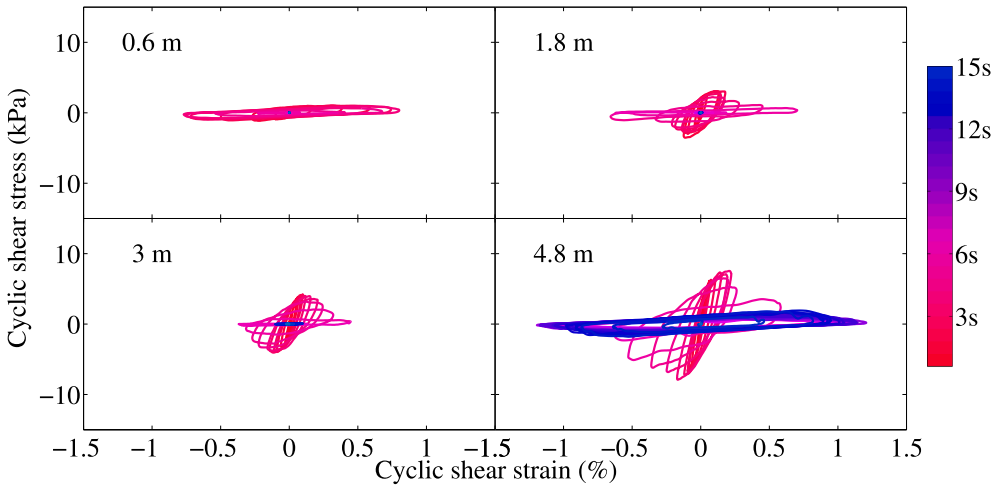

Fig. 12. Shear stress–strain loops at the selected depths (level deposit).

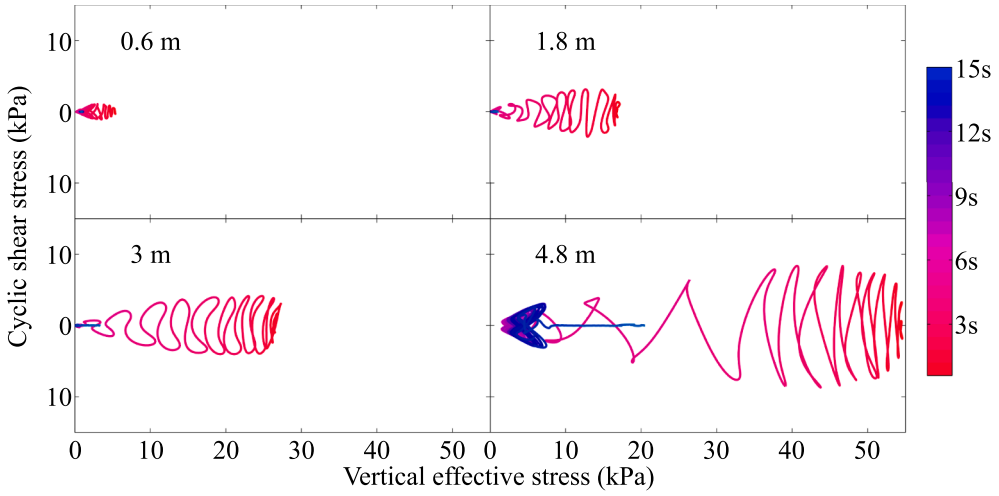

Fig. 13. Time histories of effective stress path at the selected depths (level deposit).

were considered. Therefore, for the porosity range expected in these simulations, this kernel radius would be sufficient to accurately capture the porosity at different locations. In the case of the gently sloped deposit, to mimic a mild slope of 2 degrees, the DEM and SPH particles were subjected to a gravitational acceleration which deviates from the vertical axis by 2 degrees.

According to the centrifuge scaling laws, application of a gravitational field of 30 g in the model leads to a prototype with dimensions and time scale 30 times higher than the model. Thus, the analyzed model corresponds to a periodic prototype of a 5.7 m high granular deposit with lateral dimensions of 1.44 m in each direction. The deposits were saturated with a highly viscous fluid to compensate for the effects of the employed 30 g field and comply with the scaling laws for permeability. For the prototype fluid viscosity of 0.02 Pa.s and the employed particle size range, the initial permeability of the deposit was estimated to be 2.6 mm/s (same order of coarse sand permeability when saturated with water) using the Kozeny-Carmen equation (Carman, 1937):

$$k = \frac{\rho g n^3}{5\mu(1-n)^2}\left(\frac{\sum \frac{4}{3}\pi r^3}{\sum 4\pi r^2}\right)^2 \tag{32}$$

where ρ is the fluid density, r is the equivalent particle radius, n is the average deposit porosity, and g is the gravitational acceleration. A summary of parameters used in the conducted simulations is provided in Table 1.

The deposits were subjected to sinusoidal base excitations with amplitudes of 0.01 g and 0.25 g with durations of 13 s. The sinusoidal input signal gradually increases until it reaches the maximum acceleration amplitude at 4.5 s, where it remains constant for an additional 7.5 s before it gradually decreases to zero at 13 s. The small amplitude of 0.01 g was selected as an event that was not expected to produce any significant deformations in the system. Simulations conducted with this amplitude are valuable in determination of the fundamental frequency of the deposit as well as the dynamic soil properties (shear wave velocity and low strain shear modulus). The maximum amplitude of 0.25 g represents a strong seismic event that may induce large deformations and lead to a catastrophic failure.

Applying the scaling laws for centrifuge testing results in acceleration frequencies and amplitudes that are 30 times higher in the model while the duration of the loading is 30 times smaller compared to the prototype. Several parameters at various depth locations of the deposit were monitored throughout the simulations such as averaged solid and fluid particle accelerations, averaged excess pore pressure, averaged drag force as well as stress and strain rate tensors. The data was recorded at constant time intervals of 0.0006 s in model units (0.018 s in prototype units). The simulation results provided in the following sections are in prototype units unless otherwise specified.

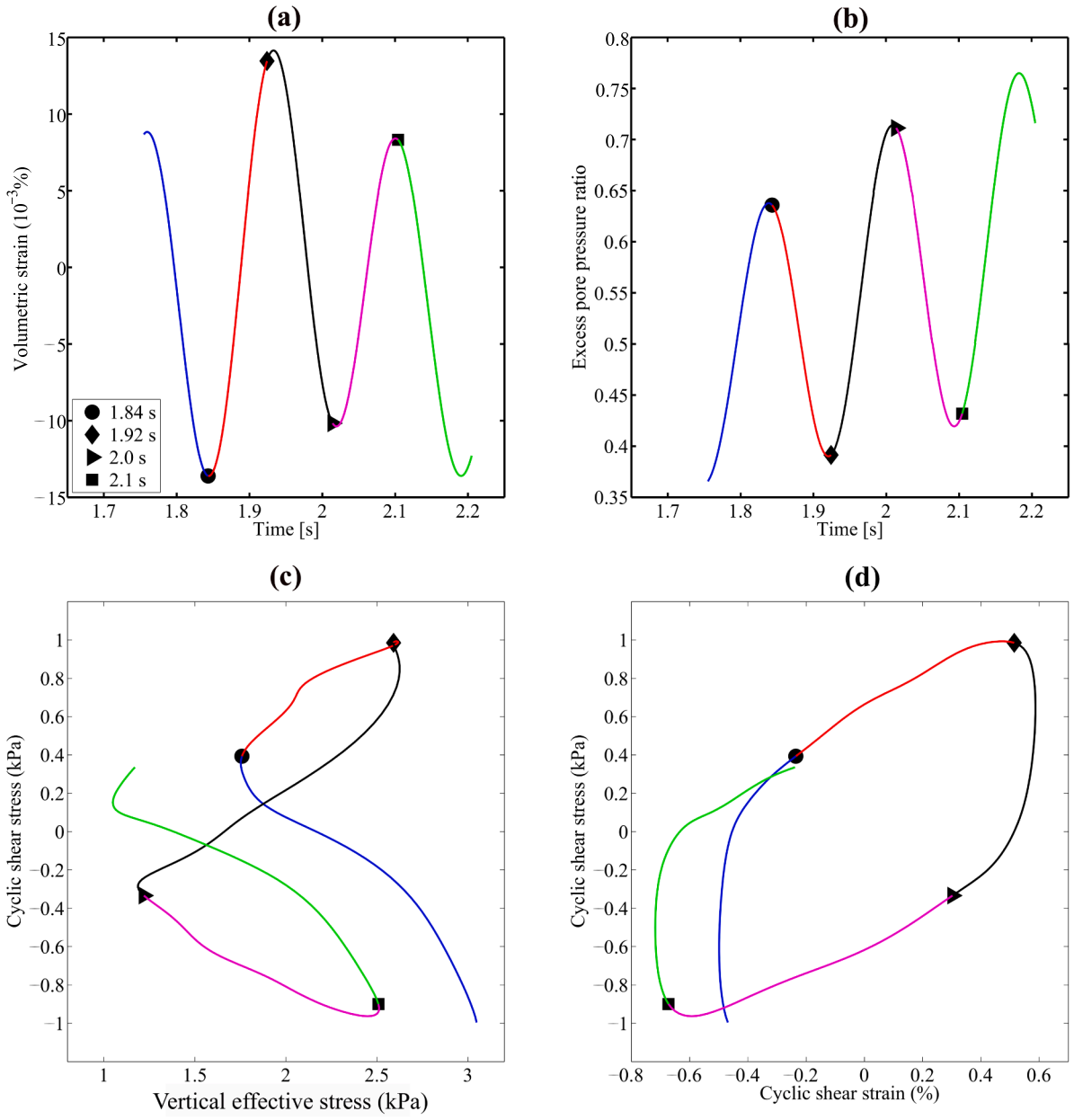

Fig. 14. Zoomed-in time window for (a) volumetric strain; (b) excess pore pressure ratio; (c) effective stress path; and (d) shear stress–strain at the depth location of 0.6 m of the level deposit.

4.2. Dynamic properties of the deposit

The shear strains induced by the base excitations with maximum amplitude of 0.01 g were in the order of 10^{-4}%. Therefore, the corresponding shear stress-shear strain loops were used to obtain the low strain shear moduli along the depth of the deposit. The average value for the low strain shear modulus was determined to be around 19.8 MPa. This means that the low strain shear wave velocity and the fundamental frequency of the deposit were approximately 100 m/s and 4.38 Hz, respectively. The amplification of the input motion toward the surface of the deposit was also observed during these simulations. The maximum amplification, as expected, occurred during the base excitation with the frequency of 4 Hz, since it was close to the fundamental frequency of the deposit. A comparison between the amplification factors at the surface of the deposit obtained form DEM simulations with maximum acceleration of 0.01 g and those of analytical expression (Kramer, 1996) for the transfer of a shear wave propagating in linear elastic soil underlain by rigid bedrock are provided in Table 2. It can be seen that there is a relatively good agreement between the results.

4.3. Liquefaction simulations

To investigate liquefaction of the granular deposits, the numerical models were subjected to strong ground motions with maximum amplitude of 0.25 g and frequency of 3 Hz. This amplitude of input motion was expected to cause enough densification of the loose deposit to cause liquefaction. From a macro-mechanical point of view, studies suggest that liquefaction is triggered by a significant buildup in the pore fluid pressure and the consequent reduction of vertical effective stress and degradation of soil strength. Several averaging volumes (measurement spheres) were created at various elevations inside the deposits. The radius of the measurement spheres was considered to be 2 cm (in model units) which is 10 times the average particle size in order to guarantee the presence of enough particles inside them. The mean fluid properties

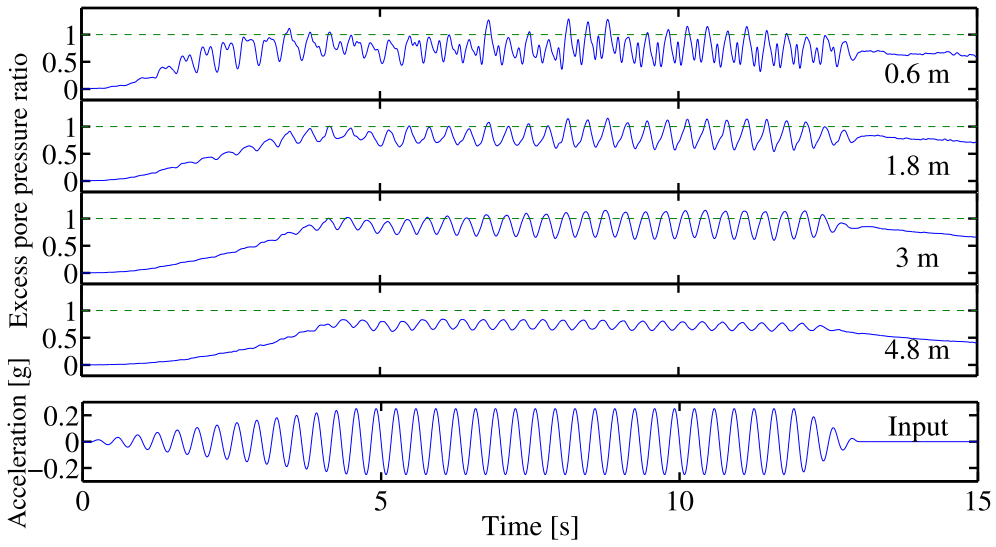

Fig. 15. Time histories of excess pore water pressure at the selected depth locations (sloping deposit).

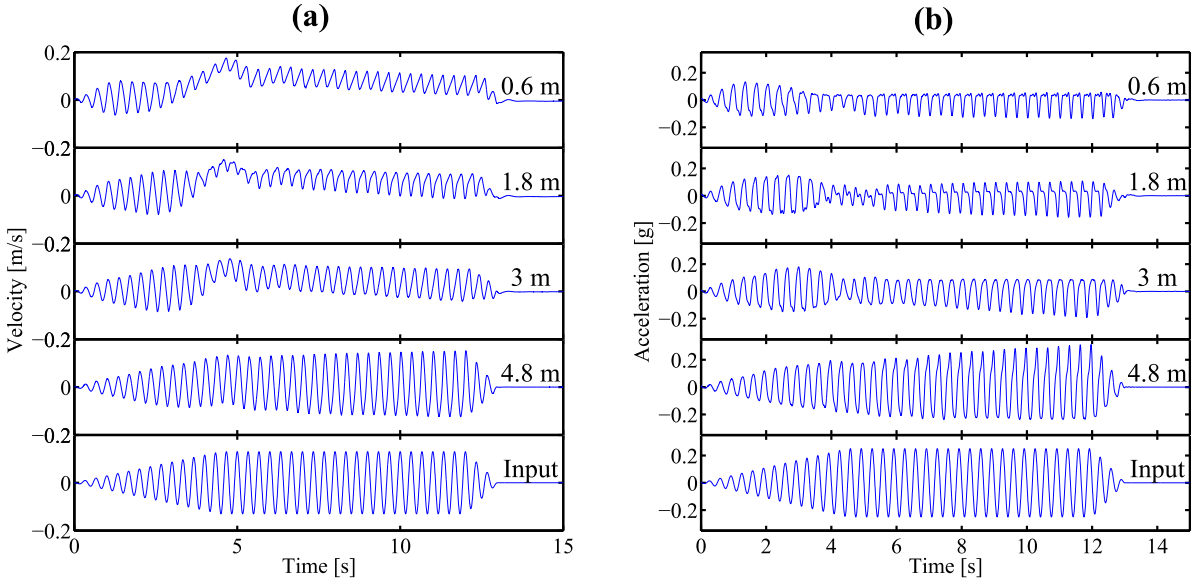

Fig. 16. Time histories of (a) average horizontal velocity and (b) average horizontal acceleration at the selected depths (sloping deposit).

were obtained by simply averaging over all SPH particles inside the measurement sphere. For more information regarding the averaging procedures for the DEM particles please see Itasca (2018). Data was collected on important variables such as pore water pressure, horizontal and vertical drag forces, average particle acceleration as well as stress and strain tensors. The results and discussions are provided in the following sections.

4.3.1. Level deposit response

The time histories of excess pore pressure ratio (the ratio of the excess pore pressure to the initial vertical effective stress) at different depth locations inside the deposit are shown in Fig. 7. Note that the presence of the particles and associated momentum transfer (Eq. (19)) as well as the gradual changes in porosity in response to shaking led to a stable pore-pressure that did not suffer from oscillation. A pore pressure ratio of 1.0 is usually used as an indicator of the occurrence of liquefaction which corresponds to a moment when the excess pore pressure counterbalances the vertical effective stress. The results show that, except for the bottom layer, the pore pressure ratio of 1.0 is practically reached during the simulation. Fig. 7 also shows that moving toward the ground surface, the pore pressure ratio increases at a higher rate. This means that liquefaction first took place near the surface and then propagated downward. These observations can also be confirmed by Fig. 8 showing the profiles of pore pressure at different times during the course of simulation. The excess pore pressure reached values close to the local vertical effective stress first in the shallow layers and as the loading continued liquefaction was spread toward the base. It can also be observed from Figs. 7 and 8 that the excess pore pressure ratio slightly decreased at the top layers after it reached the value of 1.0. This can be attributed to the proximity of these layers to the free surface and water drainage.

The average particle acceleration at different depths along the vertical axis of the deposit was recorded and is presented in Fig. 9. It was observed that the acceleration of the top 3 m of the deposit significantly diminished after the first 4 s of the base excitation. This reduction in acceleration amplitude was more evident in the upper strata where it completely vanished progressing toward the end of the simulations. These patterns are consistent with those observed in the shaking table

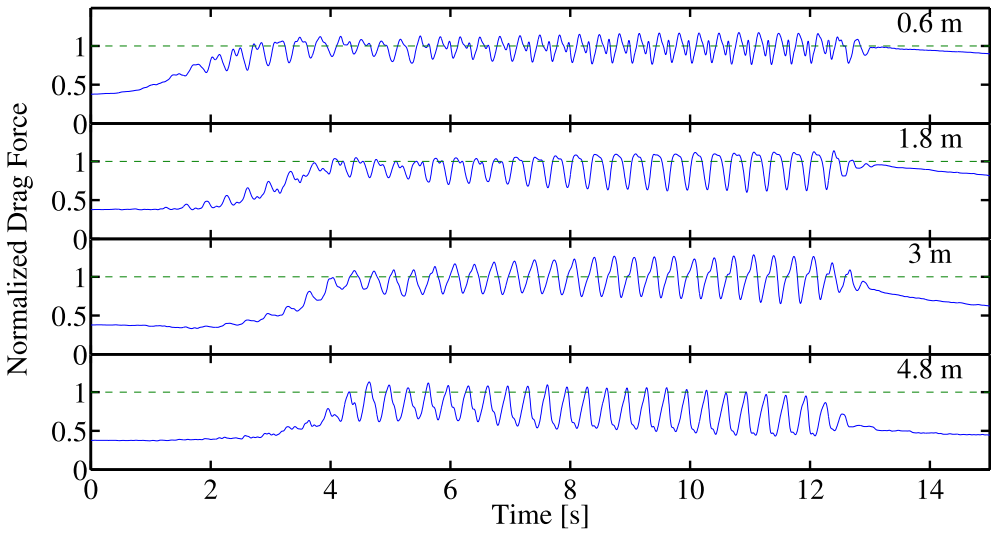

Fig. 17. Time histories of vertical fluid drag force normalized by the average particle weight at the selected depths (sloping deposit).

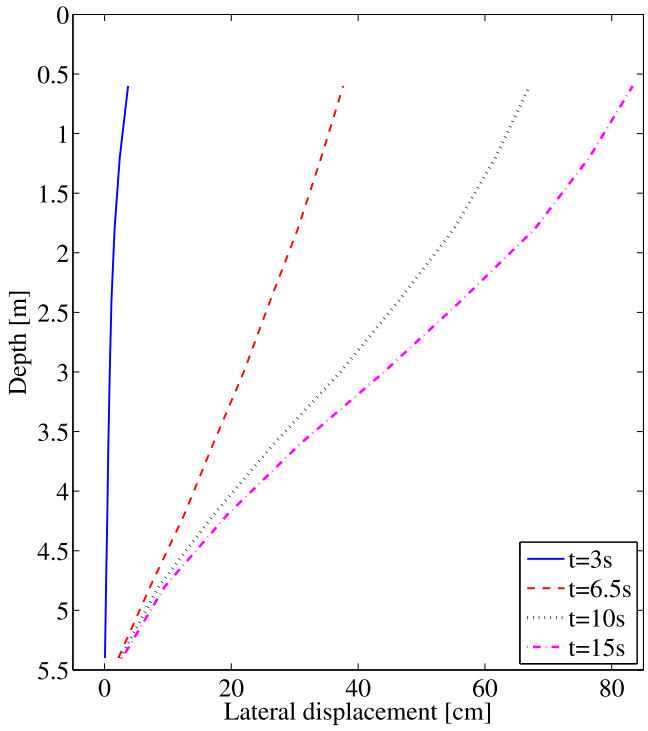

Fig. 18. Lateral displacement profiles at the selected time instants (sloping deposit).

tests and case histories of site liquefaction (e.g., Elgamal et al., 1996; Arulanandan and Scott, 1993). The drop in the acceleration amplitude was less noticeable for the depth location of 4.8 m.

To explain the observed acceleration patterns at a microscale level, the drag forces normalized by the average particle weight and the snapshots of interparticle contact chains at different time instants are provided in Figs. 10 and 11, respectively. The difference between the excess pore pressures generated inside two subsequent layers creates a pressure gradient that applies upward drag force on the particles. These forces lead to loss of some interparticle contacts. Provided that the pressure gradient is large enough, the corresponding drag forces can reach values that counterbalance the weight of particles and make them practically floating in the mixture. Fig. 10 shows that the normalized drag force drastically increased during the shaking as a result of the pore pressure buildup and reached 1.0 in all layers. However, it can be seen that at the bottom layer, while normalized drag force surpassed the value of 1.0 at several time instants, it had a considerably lower average value throughout the simulation. The significant loss of interparticle contacts can clearly be seen in Fig. 11. According to this figure, during the first few seconds of base excitation, the interparticle contacts vanished near the surface where the excess pore pressure ratio and normalized drag force first reached the value of 1.0. Fewer interparticle contacts makes soil layers only partially resting on each other and, therefore, the input excitation cannot be fully transmitted to the layers above and this leads to reduction of average particle acceleration. The same pattern was also observed at the deeper depths, except for the bottom layer, only with a time delay. At the bottom layer, as shown in Fig. 10, the drag force induced by the pressure gradient generally was not large enough to significantly reduce the number of contacts. Fig. 11 shows that after the first 4 s through the end of shaking (13 s), interparticle contacts stayed at a very low level almost in the entire deposit (except the bottom layer). This is consistent with the fact that the normalized drag force remained at its maximum level in the top layers between 4 s and 13 s (Fig. 10). It also confirms the previous observation that the acceleration amplitude almost vanished in these layers after the first 4 s of shaking. It is also worth noting that after the end of shaking (13 s), interparticle contacts significantly increased starting from the model base. This can be explained by the reduction of vertical drag force that, according to Fig. 10, first occurred at the bottom layers due to the dissipation of pore water pressure.

The cyclic shear stress–strain loops are presented in Fig. 12. For the input motion of 0.25 g, due to development of large strains, the soil behavior can no longer be considered linear and a reduction of maximum shear modulus and a shift in the natural frequency of the deposit was expected. Fig. 12 shows a progressive degradation of soil stiffness and a continuous decrease in the shear modulus at various depth locations. Fig. 13 shows the plots of cyclic shear stress versus vertical effective stress. The results show that the vertical effective stress vanished in the entire deposit by the end of the simulations except for the bottom layer.

In order to take a closer look at the liquefaction mechanism and to investigate the correlation between the different parameters, a relatively short time interval during pore pressure buildup period is selected and a point-to-point relationship between volumetric strain, excess pore pressure ratio, shear stress–strain loops and effective stress path at the depth of 0.6 m is presented in Fig. 14. It is obvious from this figure that the peaks of pore pressure correspond to the points of maximum

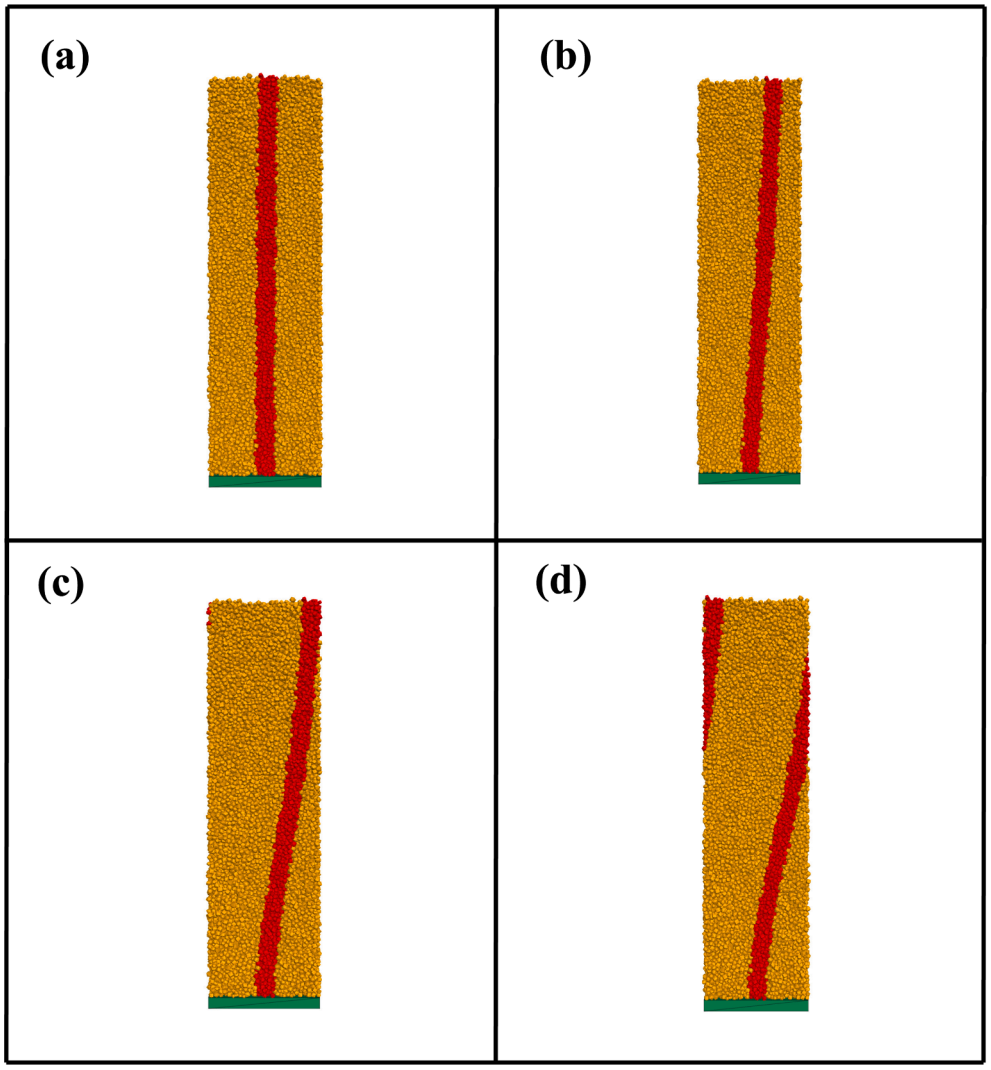

Fig. 19. Snapshots of lateral displacement profiles at (a) 3s, (b) 6s, (c) 9s, and (d) 15s (sloping deposit).

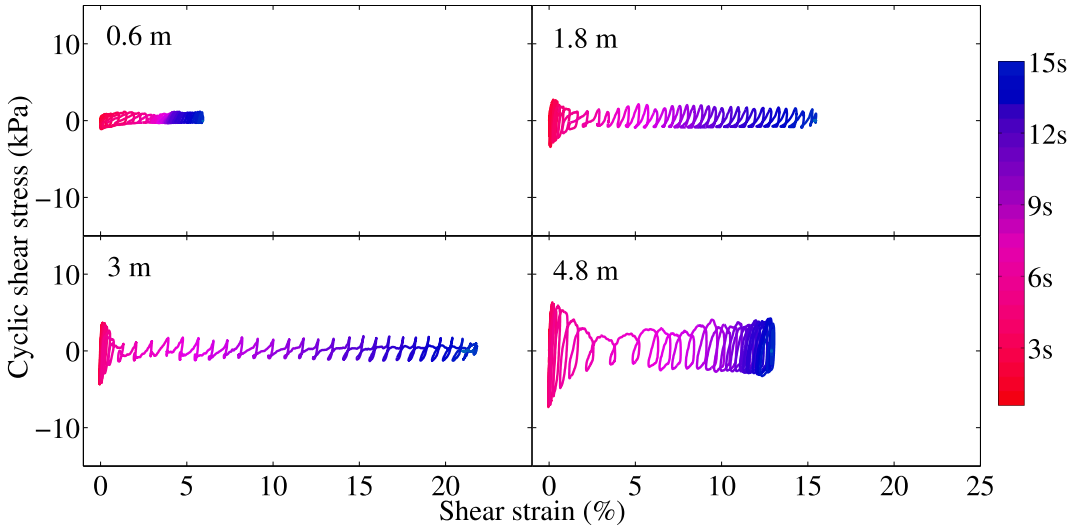

Fig. 20. Shear stress–strain loops at the selected depths (sloping deposit).

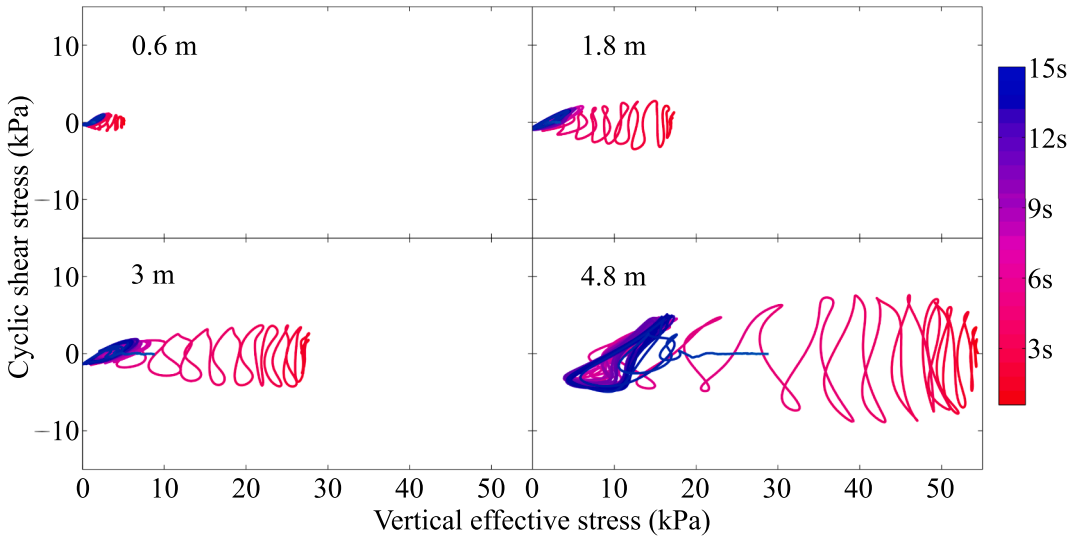

Fig. 21. Effective stress path at the selected depths (sloping deposit).

contraction (Fig. 14 a and b). In addition, pore pressure evidently drops when dilation occurs. Fig. 14(c and d) show that the vertical effective and shear stresses reached their minimum values at the points of maximum contraction due to buildup in pore pressure. On the other hand, during the dilation phase they recover to higher values and a regain in soil strength is observed. These patterns are repeatedly observed throughout the simulation.

4.3.2. *Sloping deposit response*

The previously described gently sloped deposit was subjected to the same seismic base excitation and various averaged quantities were recorded during the simulation. The time histories of pore fluid pressure at different depths are presented in Fig. 15. The patterns are similar to the level deposit response. In addition, negative spikes reflecting the dilative behavior near the surface and associated regain in soil stiffness can be observed in the time histories of pore fluid pressure at the shallow layers of the deposit. The dilative behavior is a result of particles near the surface rolling on top of each others after the onset of liquefaction and the tendency of the top layer of soil to move downslope. The time histories of averaged particle accelerations and velocities at different levels are provided in Fig. 16. The acceleration time histories suggest that the deposit demonstrated a dilative behavior reflected by a regain in shear strength and the resulting negative acceleration spikes after liquefaction occurred in the top layers. These negative sharp peaks have been observed in several computational and experimental studies (e.g., Elgamal et al., 2002; El Shamy et al., 2010). In addition, the velocity time histories show that after the onset of liquefaction, the velocities of the top layers became generally positive which means these layers were continuously moving downslope. Fig. 17 shows the plot of the normalized drag forces. It can be deduced from Fig. 17 that the top 3.0 m of the deposit liquefied during seismic excitation. It is worth noting the instantaneous gain in strength that is marked by the reduction in normalized drag force corresponding to the negative spikes in the acceleration and dips in pore pressure time histories.

The lateral spreading reflects a significant interparticle sliding at a particular depth location. As sliding takes place, the cyclic motion vanishes, and the displacement continues to increase with time as a result of the movement of the sliding mass downslope. Fig. 18 shows the computed lateral displacement profiles at various time instants. The results show relatively small lateral displacement during the first 3 s which is prior to the onset of liquefaction. For the other selected time instants, liquefaction has already occurred and large lateral displacements can be seen. The deposit experienced maximum permanent lateral displacement of around 80 cm. According to Fig. 18, the slope of the lateral spreading line has noticeably increased for the top 4 m of the deposit which completely liquefied during the simulations. A column of particles located in the middle of the deposit was colored in red for visualization purpose and the position of particles inside this column was tracked throughout the simulations. The snapshots of lateral particle displacements are also presented in Fig. 19.

The plots of shear stress versus shear strain are shown in Fig. 20. It was observed that after the first few seconds of loading, shear stresses gradually reduced and large shear strains were accumulated in the deposit. Permanent shear strains as high as 22% were observed in the liquefied layers. The loops also show the instantaneous gain in stiffness (marked by the steep increase in shear stress) as the soil dilates even after the onset of liquefaction corresponding to the negative spikes observed in the acceleration and pore pressure time histories (Fig. 16). The effective stress paths are shown in Fig. 21. The results show that, apart from the bottom layer, the zero value for the vertical effective stress was reached. It also shows indications of dilative behavior marked by the regain of effective stress as it was approaching zero in top layers. Note the non-symmetric shape of the effective stress path due to the static component of shear stress in the slope direction.

Fig. 22 presents a point-to-point relationship between cyclic volumetric strain, excess pore pressure ratio, effective stress path and shear stress–strain loops at the depth of 0.6 m over a short time window during the simulation of the sloping deposit. Here, the time interval is chosen near the end of shaking to investigate the previously mentioned dips and peaks observed in the time histories of excess pore pressure. Similar to what was observed for the level deposit, the contraction of the pore spaces leads to an increase in the pore pressure and, conversely, the dips in pore pressure correspond to the points of peak dilation (Fig. 22 a and b). Dilatation occurs as the soil mass is moving upslope while contraction occurs mostly as the mass is moving downslope (El Shamy and Abdelhamid, 2017). Fig. 22(c and d) show that the vertical effective and shear stresses reached their minimum values at the points of maximum contraction. In addition, regains in the soil strength clearly corresponds to the points of maximum dilation. Peaks of excess pore pressure correspond to near-complete loss of soil strength marked by the significant reduction in vertical effective stress (Fig. 22 b and c).

5. Conclusions

A three-dimensional Lagrangian-Lagrangian approach is utilized to analyze the dynamic response and liquefaction of saturated level and gently sloped granular deposits. A microscale idealization of the solid phase is achieved using the discrete element method. Considering the

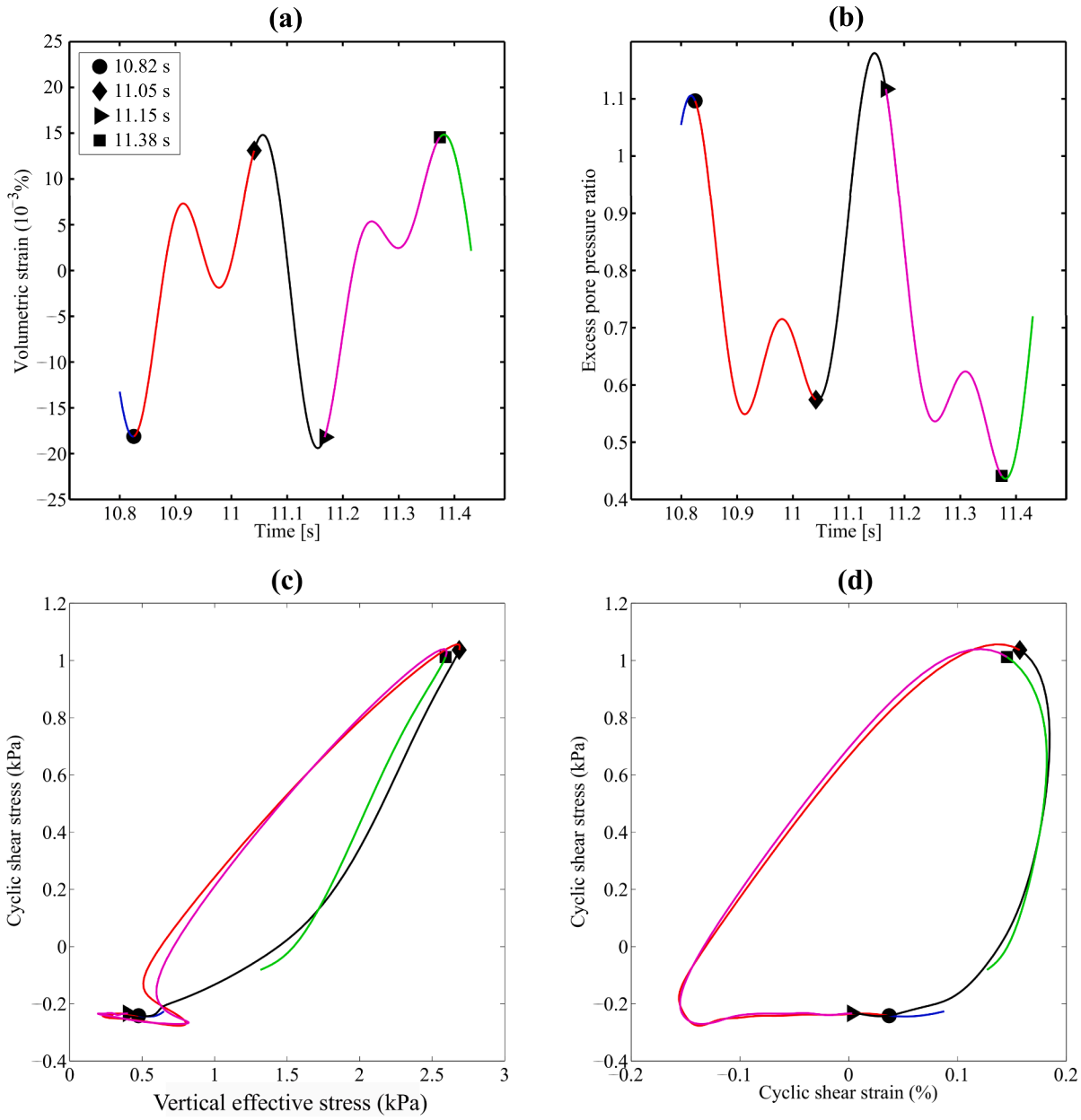

Fig. 22. Zoomed-in time window for (a) volumetric strain; (b) excess pore pressure ratio; (c) effective stress path; and (d) shear stress–strain at the depth location of 0.6 m of the sloping deposit.

non-sphericity of real soil grains, irregular-shaped particles are chosen as the most realistic representation of the soil particles. The fluid phase is modeled using the smoothed particle hydrodynamics. In this method, the interstitial pore fluid is idealized using averaged Navier–Stokes equations and the fluid-particle interaction forces are quantified using well-known semi-empirical relationships. The presented model is computationally far less demanding compared to the pore-scale level models and its meshless nature makes it a powerful tool for analyzing moving boundary and free surface problems. In addition, the presented model is seamlessly capable of predicting the response at small and large strains. The proposed approach was used to model the response of saturated soil deposits subjected to seismic excitation. The results show that liquefaction took place in both deposits marked by several response mechanisms including excess pore-pressure buildup approaching the value of one, increase in the vertical drag forces that counterbalance the weight of solid particles, reduction of interparticle contacts causing the instability of the packing, diminishing averaged particle acceleration time histories and continuous degradation of soil stiffness and strength. Large lateral displacements were observed during the sloping deposit simulation as a result of the sliding of liquefied soil layers downslope. A dilative behavior was observed in the shallow layers of the gently sloped deposit reflected by sharp negative acceleration and pore fluid pressure dips after the occurrence of liquefaction and nonsymmetric loops in the effective stress path plots as the mean vertical effective stress approached zero. The macro-mechanical behavior of the numerical model exhibits similar trends to those observed in published experimental studies and case histories of soil liquefaction.

CRediT authorship contribution statement

Saman Farzi Sizkow: Software, Formal analysis, Data curation, Visualization, Writing - original draft. **Usama El Shamy:** Conceptualization, Methodology, Investigation, Supervision, Writing - review & editing.

Declaration of Competing Interest

The authors declare that they have no known competing financial interests or personal relationships that could have appeared to influence the work reported in this paper.

Acknowledgments

This research was partially supported by the US Army Corps of Engineers Engineer Research and Development Center, Grant No. W9132V-13-C-0004 and the National Science Foundation award number CMMI-1728612. These supports are gratefully acknowledged.

References

Abdelhamid, Y., El Shamy, U., 2016. Pore-scale modeling of fine-particle migration in granular filters. Int. J. Geomech. 16 (3), 04015086.
Adami, S., Hu, X.Y., Adams, N.A., 2012. A generalized wall boundary condition for smoothed particle hydrodynamics. J. Comput. Phys. 231 (21), 7057–7075.
Anderson, T.B., Jackson, R., 1967. Fluid mechanical description of fluidized beds. equations of motion. Indust. Eng. Chem. Fundam. 6 (4), 527–539.
Andrade, J.E., 2009. A predictive framework for liquefaction instability. Géotechnique 59 (8), 673–682.
Arulanandan, K., Scott, R.F., 1993. Verification of numerical procedures for the analysis of soil liquefaction problems. In: International Conference on the Verification of Numerical Procedures for the Analysis of Soil Liquefaction Problems (1993: Davis, Calif.). AA Balkema.
Bardet, J.P., 1994. Observations on the effects of particle rotations on the failure of idealized granular materials. Mech. Mater. 18 (2), 159–182.
Bardet, J.P., Huang, Q., 1992. Numerical modeling of micropolar effects in idealized granular materials. Mech. Granular Mater. Powder Syst. 37, 85–91.
Borja, R.I., 2006. Condition for liquefaction instability in fluid-saturated granular soils. Acta Geotech. 1 (4), 211.
Borja, R.I., Chao, H.Y., Montáns, F.J., Lin, C.H., 1999. SSI effects on ground motion at Lotung LSST site. J. Geotech. Geoenviron. Eng. 125 (9), 760–770.
Boulanger, R.W., Ziotopoulou, K., 2013. Formulation of a sand plasticity plane-strain model for earthquake engineering applications. Soil Dyn. Earthq. Eng. 53, 254–267.
Calvetti, F., Combe, G., Lanier, J., 1997. Experimental micromechanical analysis of a 2D granular material: relation between structure evolution and loading path. Mech. Cohesive-frictional Mater.: Int. J. Exp., Modell. Comput. Mater. Struct. 2 (2), 121–163.
Carman, P.C., 1937. Fluid flow through granular beds. Trans. Inst. Chem. Eng. 15, 150–166.
Cavarretta, I., Coop, M., O'Sullivan, C., 2010. The influence of particle characteristics on the behaviour of coarse grained soils. Géotechnique 60 (6), 413–423.
Chang, S.W., Chen, C.S., 2008. A non-iterative derivation of the common plane for contact detection of polyhedral blocks. Int. J. Numer. Meth. Eng. 74 (5), 734–753.
Chen, J.K., Beraun, J.E., Carney, T.C., 1999. A corrective smoothed particle method for boundary value problems in heat conduction. Int. J. Numer. Meth. Eng. 46 (2), 231–252.
Cleary, P.W., 2015. Prediction of coupled particle and fluid flows using DEM and SPH. Miner. Eng. 73, 85–99.
Crespo, A.J.C., Gómez-Gesteira, M., Dalrymple, R.A., 2007. 3D SPH simulation of large waves mitigation with a dike. J. Hydraul. Res. 45 (5), 631–642.
Cubrinovski, M., Bradley, B., Wotherspoon, L., Green, R., Bray, J., Wood, C., Pender, M., Allen, J., Bradshaw, A., Rix, G., et al., 2011. Geotechnical aspects of the 22 February 2011 Christchurch earthquake. Bull. New Zeal. Soc. Earthq. Eng. 44 (4), 205–226.
Cundall, P.A., 1988. Formulation of a three-dimensional distinct element model-Part I. A scheme to detect and represent contacts in a system composed of many polyhedral blocks. In: International Journal of Rock Mechanics and Mining Sciences & Geomechanics Abstracts, vol. 25. Pergamon, pp. 107–116.
Dafalias, Y, 1982. Bounding surface formulation of soil plasticity. Soil Mech.-Transient Cyclic Loads 253–282.
Dehnen, W., Aly, H., 2012. Improving convergence in smoothed particle hydrodynamics simulations without pairing instability. Mon. Not. R. Astron. Soc. 425 (2), 1068–1082.
Desai, C.S., Siriwardane, H.J., 1984. Constitutive Laws for Engineering Materials with Emphasis on Geologic Materials. Prentice-Hall.
El Shamy, U., Abdelhamid, Y., 2014. Modeling granular soils liquefaction using coupled lattice Boltzmann method and discrete element method. Soil Dyn. Earthq. Eng. 67, 119–132.
El Shamy, U., Abdelhamid, Y., 2017. Some aspects of the impact of multidirectional shaking on liquefaction of level and sloping granular deposits. J. Eng. Mech. 143 (1), C4016003.
El Shamy, U., Aydin, F., 2008. Multiscale modeling of flood-induced piping in river levees. J. Geotech. Geoenviron. Eng. 134 (9), 1385–1398.
El Shamy, U., Denissen, C., 2010. Microscale characterization of energy dissipation mechanisms in liquefiable granular soils. Comput. Geotech. 37 (7–8), 846–857.
El Shamy, U., Sizkow, S.F., 2021. Coupled smoothed particle hydrodynamics-discrete element method simulations of soil liquefaction and its mitigation using gravel drains. Soil Dyn. Earthq. Eng. https://doi.org/10.1016/j.soildyn.2020.106460.
El Shamy, U., Zeghal, M., 2005. Coupled continuum-discrete model for saturated granular soils. J. Eng. Mech. 131 (4), 413–426.
El Shamy, U., Zeghal, M., Dobry, R., Thevanayagam, S., Elgamal, A., Abdoun, T., Medina, C., Bethapudi, R., Bennett, V., 2010. Micromechanical aspects of liquefaction-induced lateral spreading. Int. J. Geomech. 10 (5), 190–201.
Elgamal, A., Yang, Z., Parra, E., 2002. Computational modeling of cyclic mobility and post-liquefaction site response. Soil Dyn. Earthq. Eng. 22 (4), 259–271.
Elgamal, A.W., Zeghal, M., Parra, E., 1996. Liquefaction of reclaimed island in Kobe, Japan. J. Geotech. Eng. 122 (1), 39–49.
Erdik, M, 2000. Report on 1999 Kocaeli and Düzce (Turkey) Earthquakes. Boğaziçi Üniversitesi, Kandilli Rasathanesi ve Deprem Araştirma Enstitüsü.
Ergun, S., 1952. Fluid flow through packed columns. Chem. Eng. Prog. 48, 89–94.
Fernandez, J.W., Cleary, P.W., Sinnott, M.D., Morrison, R.D., 2011. Using SPH one-way coupled to DEM to model wet industrial banana screens. Miner. Eng. 24 (8), 741–753.
Foroutan, T., Mirghasemi, A.A., 2020. CFD-DEM model to assess stress-induced anisotropy in undrained granular material. Comput. Geotech. 119, 103318.
Gingold, R.A., Monaghan, J.J., 1977. Smoothed particle hydrodynamics: theory and application to non-spherical stars. Mon. Not. R. Astron. Soc. 181 (3), 375–389.
Gómez-Gesteira, M., Cerqueiro, D., Crespo, C., Dalrymple, R.A., 2005. Green water overtopping analyzed with a SPH model. Ocean Eng. 32 (2), 223–238.
Gong, G., Thornton, C., Chan, A.H.C., 2012. DEM simulations of undrained triaxial behavior of granular material. J. Eng. Mech. 138 (6), 560–566.
Gu, X., Zhang, J., Huang, X., 2020. DEM analysis of monotonic and cyclic behaviors of sand based on critical state soil mechanics framework. Comput. Geotech. 128, 103787.
Han, K., Feng, Y.T., Owen, D.R.J., 2007. Numerical simulations of irregular particle transport in turbulent flows using coupled LBM-DEM. Comput. Model. Eng. Sci. 18 (2), 87.
Han, Y., Cundall, P.A., 2011. Lattice Boltzmann modeling of pore-scale fluid flow through idealized porous media. Int. J. Numer. Meth. Fluids 67 (11), 1720–1734.
Huang, X., Hanley, K.J., Zhang, Z., Kwok, C., 2019. Structural degradation of sands during cyclic liquefaction: Insight from DEM simulations. Comput. Geotech. 114, 103139.
Huang, X., Xu, M., Zhang, Z., Lei, Q., 2020. Characterizing stress variability within granular samples upon liquefaction. Comput. Geotech. 127, 103771.
Iai, S., Tobita, T., Nakahara, T., 2005. Generalised scaling relations for dynamic centrifuge tests. Geotechnique 55 (5), 355–362.
Itasca, 2018. PFC3D (Particle Flow Code in 3 Dimensions), version 6.0. ICG, Minneapolis.
Iwashita, K., Oda, M., 1998. Rolling resistance at contacts in simulation of shear band development by DEM. J. Eng. Mech. 124 (3), 285–292.
Jiang, M., Chen, H., Tapias, M., Arroyo, M., Fang, R., 2014. Study of mechanical behavior and strain localization of methane hydrate bearing sediments with different saturations by a new DEM model. Comput. Geotech. 57, 122–138.
Jie, Ying, Tang, Xiaowei, Luan, Maotian, Yang, Qing, 2008. Adaptive element free Galerkin method applied to analysis of earthquake induced liquefaction. Earthq. Eng. Eng. Vib. 7 (2), 217–224.
Johnson, D.H., Vahedifard, F., Jelinek, B., Peters, J.F., 2017. Micromechanics of undrained response of dilative granular media using a coupled DEM-LBM model: a case of biaxial test. Comput. Geotech. 89, 103–112.
Karunasena, H.C.P., Senadeera, W., Gu, Y.T., Brown, R.J., 2014. A coupled SPH-DEM model for micro-scale structural deformations of plant cells during drying. Appl. Math. Model. 38 (15–16), 3781–3801.
Klisiński, M., 1988. Plasticity theory based on fuzzy sets. J. Eng. Mech. 114 (4), 563–582.
Kramer, S., 1996. Geotechnical Earthquake Engineering. Prentice Hall, New Jersey.
Kuhn, M.R., Renken, H.E., Mixsell, A.D., Kramer, S.L., 2014. Investigation of cyclic liquefaction with discrete element simulations. J. Geotech. Geoenviron. Eng. 140 (12), 04014075.
Liang, K., Ren, P., 2011. Particle flow simulation of influence of particle shape on mechanical properties of quasi-sands. Chinese J. Rock Mech. Eng. 30 (10), 2112–2119.
Lucy, L.B., 1977. A numerical approach to the testing of the fission hypothesis. Astronom. J. 82, 1013–1024.
Madabhushi, S.P.G., Zeng, X., 1998. Seismic response of gravity quay walls. II: Numerical modeling. J. Geotech. Geoenviron. Eng. 124 (5), 418–427.
Markauskas, D., Kruggel-Emden, H., 2019. Coupled DEM-SPH simulations of wet continuous screening. Adv. Powder Technol. 30 (12), 2997–3009.
Markauskas, D., Kruggel-Emden, H., Sivanesapillai, R., Steeb, H., 2017. Comparative study on mesh-based and mesh-less coupled CFD-DEM methods to model particle-laden flow. Powder Technol. 305, 78–88.
Markauskas, D., Kruggel-Emden, H., Scherer, V., 2018. Numerical analysis of wet plastic particle separation using a coupled DEM-SPH method. Powder Technol. 325, 218–227.
Martin, E.L., Thornton, C., Utili, S., 2019. Micromechanical investigation of liquefaction of granular media by cyclic 3D DEM tests. Géotechnique 1–10.
Misra, A., Jiang, H., 1997. Measured kinematic fields in the biaxial shear of granular materials. Comput. Geotech. 20 (3–4), 267–285.
Monaghan, J.J., 1992. Smoothed particle hydrodynamics. Ann. Rev. Astron. Astrophys. 30 (1), 543–574.
Monaghan, J.J., 1994. Simulating free surface flows with SPH. J. Comput. Phys. 110 (2), 399–406.
Monaghan, J.J., 2000. SPH without a tensile instability. J. Comput. Phys. 159 (2), 290–311.
Morris, J.P., Fox, P.J., Zhu, Y., 1997. Modeling low Reynolds number incompressible flows using SPH. J. Comput. Phys. 136 (1), 214–226.

Naili, M., Matsushima, T., Yamada, Y., 2005. A 2D smoothed particle hydrodynamics method for liquefaction induced lateral spreading analysis. J. Appl. Mech. 8, 591–599.
Nezami, E.G., Hashash, Y., Zhao, D., Ghaboussi, J., 2004. A fast contact detection algorithm for 3-D discrete element method. Comput. Geotech. 31 (7), 575–587.
Nezami, E.G., Hashash, Y., Zhao, D., Ghaboussi, J., 2006. Shortest link method for contact detection in discrete element method. Int. J. Numer. Anal. Meth. Geomech. 30 (8), 783–801.
Ng, T.T., Dobry, R., 1994. Numerical simulations of monotonic and cyclic loading of granular soil. J. Geotech. Eng. 120 (2), 388–403.
Oda, M., Konishi, J., Nemat-Nasser, S., 1982. Experimental micromechanical evaluation of strength of granular materials: effects of particle rolling. Mech. Mater. 1 (4), 269–283.
Ong, C.J., Gilbert, E.G., 1997. The Gilbert-Johnson-Keerthi distance algorithm: a fast version for incremental motions. In: Proceedings of International Conference on Robotics and Automation, vol. 2. IEEE, pp. 1183–1189.
Pena, A.A., Garcia-Rojo, R., Herrmann, H.J., 2007. Influence of particle shape on sheared dense granular media. Granular Matter 9 (3–4), 279–291.
Potapov, A.V., Hunt, M.L., Campbell, C.S., 2001. Liquid–solid flows using smoothed particle hydrodynamics and the discrete element method. Powder Technol. 116 (2–3), 204–213.
Prevost, J.H., 1985. A simple plasticity theory for frictional cohesionless soils. Int. J. Soil Dyn. Earthq. Eng. 4 (1), 9–17.
Randles, P.W., Libersky, L.D., 1996. Smoothed particle hydrodynamics: some recent improvements and applications. Comput. Methods Appl. Mech. Eng. 139 (1–4), 375–408.
Ravichandran, N., Machmer, B., Krishnapillai, H., Meguro, K., 2010. Micro-scale modeling of saturated sandy soil behavior subjected to cyclic loading. Soil Dyn. Earthq. Eng. 30 (11), 1212–1225.
Regueiro, R.A., Borja, R.I., 1999. A finite element model of localized deformation in frictional materials taking a strong discontinuity approach. Finite Elem. Anal. Des. 33 (4), 283–315.
Robinson, M., Ramaioli, M., Luding, S., 2014. Fluid–particle flow simulations using two-way-coupled mesoscale SPH–DEM and validation. Int. J. Multiph. Flow 59, 121–134.
Salimi, M.J., Lashkari, A., 2020. Undrained true triaxial response of initially anisotropic particulate assemblies using cfm-dem. Comput. Geotech. 124, 103509.
Sato, K., Kokusho, T., Matsumoto, M., Yamada, E., 1995. Nonlinear seismic response and soil property during 1995 Hyogoken Nanbu earthquake. Soils Found. Special Issue Geotech. Aspects 17, 41–52.
Seed, R.B., Dickenson, S.E., Idriss, I.M., 1991. Principal geotechnical aspects of the 1989 Loma Prieta earthquake. Soils Found. 31 (1), 1–26.
Seid-Karbasi, M., Byrne, P.M., 2007. Seismic liquefaction, lateral spreading, and flow slides: a numerical investigation into void redistribution. Can. Geotech. J. 44 (7), 873–890.
Shafipour, R., Soroush, A., 2008. Fluid coupled-DEM modelling of undrained behavior of granular media. Comput. Geotech. 35 (5), 673–685.
Shamos, M.I., Hoey, D., 1976. Geometric intersection problems. In: 17th Annual Symposium on Foundations of Computer Science. IEEE, pp. 208–215.
Shin, H., Santamarina, J.C., 2013. Role of particle angularity on the mechanical behavior of granular mixtures. J. Geotech. Geoenviron. Eng. 139 (2), 353–355.
Sinnott, M.D., Cleary, P.W., Morrison, R.D., 2017. Combined DEM and SPH simulation of overflow ball mill discharge and trommel flow. Miner. Eng. 108, 93–108.
Sitharam, T.G., Vinod, J.S., Ravishankar, B.V., 2009. Post-liquefaction undrained monotonic behaviour of sands: experiments and dem simulations. Géotechnique 59 (9), 739–749.
Kenichi Soga, E., Alonso, Alba Yerro, Kumar, K., Bandara, Samila, 2016. Trends in large-deformation analysis of landslide mass movements with particular emphasis on the material point method. Géotechnique 66 (3), 248–273.
Sun, X., Sakai, M., Yamada, Y., 2013. Three-dimensional simulation of a solid–liquid flow by the DEM–SPH method. J. Comput. Phys. 248, 147–176.
Szarf, K., Combe, G., Villard, P, 2009. Influence of the grains shape on the mechanical behavior of granular materials. In: AIP Conference Proceedings, vol. 1145. American Institute of Physics, pp. 357–360.
Tasiopoulou, P., Gerolymos, N., 2016. Constitutive modelling of sand: a progressive calibration procedure accounting for intrinsic and stress-induced anisotropy. Géotechnique 66 (9), 754–770.
Trussell, R.R., Chang, M., 1999. Review of flow through porous media as applied to head loss in water filters. J. Environ. Eng. 125 (11), 998–1006.
Wachs, A., Girolami, L., Vinay, G., Ferrer, G., 2012. Grains3D, a flexible DEM approach for particles of arbitrary convex shape-Part I: Numerical model and validations. Powder Technol. 224, 374–389.
Wang, G., Wei, J., 2016. Microstructure evolution of granular soils in cyclic mobility and post-liquefaction process. Granular Matter 18 (3), 51.
Wang, R., Zhang, J.M., Wang, G., 2014. A unified plasticity model for large post-liquefaction shear deformation of sand. Comput. Geotech. 59, 54–66.
Wang, R., Fu, P., Zhang, J., Dafalias, Y.F., 2019. Fabric characteristics and processes influencing the liquefaction and re-liquefaction of sand. Soil Dyn. Earthq. Eng. 125, 105720.
Wei, Haoyan, Chen, Jiun-Shyan, Beckwith, Frank, Baek, Jonghyuk, 2020. A naturally stabilized semi-lagrangian meshfree formulation for multiphase porous media with application to landslide modeling. J. Eng. Mech. 146 (4), 04020012.
Wei, J., Huang, D., Wang, G., 2018. Microscale descriptors for particle-void distribution and jamming transition in pre-and post-liquefaction of granular soils. J. Eng. Mech. 144 (8), 04018067.
Wood, D.M., 1990. Soil Behaviour and Critical State Soil Mechanics. Cambridge University Press.
Wu, K., Yang, D., Wright, N., 2016. A coupled SPH-DEM model for fluid-structure interaction problems with free-surface flow and structural failure. Comput. Struct. 177, 141–161.
Yamaguchi, Yuya, Takase, Shinsuke, Moriguchi, Shuji, Terada, Kenjiro, 2020. Solid–liquid coupled material point method for simulation of ground collapse with fluidization. Comput. Particle Mech. 7 (2), 209–223.
Zhong, W., Yu, A., Liu, X., Tong, Z., Zhang, H., 2016. DEM/CFD-DEM modelling of non-spherical particulate systems: theoretical developments and applications. Powder Technol. 302, 108–152.
Zhou, B., Huang, R., Wang, H., Wang, J., 2013. DEM investigation of particle anti-rotation effects on the micromechanical response of granular materials. Granular Matter 15 (3), 315–326.
Zhu, Y.I., Fox, P.J., Morris, J.P., 1999. A pore-scale numerical model for flow through porous media. Int. J. Numer. Anal. Meth. Geomech. 23 (9), 881–904.
Ziotopoulou, K., Boulanger, R.W., 2013. Calibration and implementation of a sand plasticity plane-strain model for earthquake engineering applications. Soil Dyn. Earthq. Eng. 53, 268–280.